SIAM J. SCI. COMPUT.
Vol. 47, No. 5, pp. B1077–B1103

AN EFFICIENT HIGH-ORDER COMPACT SPLITTING SPECTRAL METHOD FOR DIPOLAR BOSE-EINSTEIN CONDENSATES WITH ARBITRARY-ANGLE ROTATION*

XIN LIU† AND YONG ZHANG‡

Abstract. We propose high-order compact splitting Fourier spectral methods to compute the dynamics of dipolar Bose–Einstein condensates (BECs) with arbitrary-angle rotation. The Hamiltonian is split into a linear part that consists of the Laplace and rotation and a nonlinear part that includes all the remaining terms. For the linear subproblem, we factorize the linear operator into a product of simple suboperators using the exact classical-quantum correspondence and semigroups decomposition, and these suboperators are integrated exactly in either physical or phase space. Importantly, we first derive explicit formulas for the splitting coefficients originally obtained by numerically solving a nonlinear system. The nonlinear part is solved exactly in physical space, and the convolution-type nonlocal potential with a singular kernel is computed via the Far-field Smooth Approximation (FSA) method with spectral accuracy. This "compact" splitting, involving only two operators, significantly simplifies the design of high-order schemes. Our method achieves high-order temporal precision and spectral spatial accuracy with near-optimal efficiency, and it is explicit, easy to implement and unconditionally stable. In addition, we derive some dynamical properties and conduct a comprehensive investigation, including accuracy confirmation, property verification, interaction of quantized vortices, and dynamics under honeycomb potential.

Key words. Bose-Einstein condensate, arbitrary-angle rotation, nonlocal potential, dynamics, high order operator splitting scheme

MSC codes. 35Q41, 65M70, 81Q05, 81V45

DOI. 10.1137/24M1716069

1. Introduction.

The experimental achievement of Bose–Einstein condensation (BEC) of dilute gases in 1995 [3] opened a new era in atomic, molecular, and optical physics and quantum optics and offered an incredible glimpse into the macroscopic quantum world. Later, the observation of quantized vortices [1], a hallmark of the superfluid nature of BEC, garnered widespread attention and sparked extensive research on rotating BEC. Early experiments mainly focused on cold atomic gases, whose properties are primarily governed by isotropic and short-range interatomic interactions. With advancements in experimental techniques, BECs of dipolar quantum gases, such as ^{52}Cr [17], ^{164}Dy [25], and ^{168}Er [2], have been successfully realized. These systems, characterized by anisotropic and long-range magnetic/electric dipole-dipole interactions (DDI), have spurred great enthusiasm within the atomic physics community.

Early experiments on rotating BEC focused on systems rotating along the z-axis. However, real-world applications may demand rotation at arbitrary angles.

*Submitted to the journal's Software, High-Performance Computing, and Computational Science and Engineering section December 9, 2024; accepted for publication (in revised form) June 21, 2025; published electronically September 17, 2025.

https://doi.org/10.1137/24M1716069

Funding: This work was supported by the National Natural Science Foundation of China (12271400) and Basic Research Fund of Tianjin University (Grant 2025XJ21-0010).

†Center for Applied Mathematics and KL-AAGDM, Tianjin University, Tianjin, 300072 China (liuxin_0921@tju.edu.cn).

‡Corresponding author. Center for Applied Mathematics and KL-AAGDM, Tianjin University, Tianjin, 300072 People's Republic of China (sunny5zhang@gmail.com).

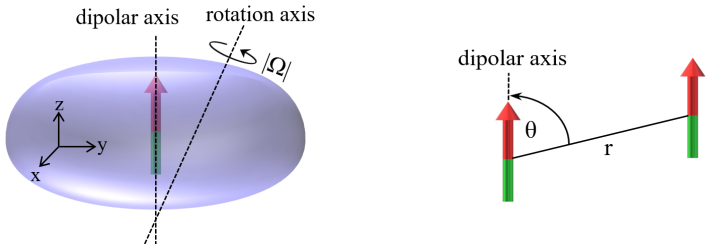

FIG. 1. *Intuitive picture for a dipolar BEC with arbitrary-angle rotation (left) and two particles interacting via the dipole-dipole interaction (right), where* $r = |\mathbf{x}|$ *denotes the distance between two dipoles* [20].

For example, a BEC confined by a rotating harmonic trap whose the rotation axis is not aligned with any of its principle axes and arbitrary-angle rotation of the polarization of a dipolar BEC have been investigated in [28, 27]. In addition, when the rotation axis differs from the alignment of dipoles (commonly along the z-axis due to an external field), as shown in Figure 1, the interplay between rotational dynamics and DDI can give rise to several intriguing phenomena. Consequently, BECs with arbitrary-angle rotation represents a fascinating subject in the field of quantum physics [27, 28, 31, 32].

At temperatures T much lower than the critical temperature T_c, the properties of BEC in a rotating frame with long-range DDI are well described by the macroscopic complex-valued wave function $\psi(\mathbf{x}, t)$. The evolution of the wave function is governed by the three-dimensional (3D) Gross-Pitaevskii equation (GPE) with an angular momentum rotation term and DDI. In dimensionless form, the 3D GPE is expressed as follows [5, 6, 31, 33]:

$$i\partial_t \psi(\mathbf{x}, t) = \left[-\frac{1}{2}\Delta + V(\mathbf{x}) + \beta|\psi|^2 + \lambda\Phi(\mathbf{x}, t) - \boldsymbol{\Omega}\cdot\boldsymbol{L}\right]\psi(\mathbf{x}, t), \tag{1.1}$$

$$\Phi(\mathbf{x}, t) = (U_{\text{dip}} * |\psi|^2)(\mathbf{x}, t), \tag{1.2}$$

$$\psi(\mathbf{x}, 0) = \psi^0(\mathbf{x}). \tag{1.3}$$

Here, $\mathbf{x} = (x, y, z)^\top \in \mathbb{R}^3$, t is the time, and $*$ represents the convolution operator with respect to the spatial variables. The vector $\boldsymbol{\Omega} = (\omega_x, \omega_y, \omega_z)^\top \in \mathbb{R}^3$ represents the angular velocity vector and the angular momentum operator $\boldsymbol{L} = \mathbf{x} \wedge (-i\nabla) = (L_x, L_y, L_z)^\top$ with

$$L_x = -i(y\partial_z - z\partial_y), \quad L_y = -i(z\partial_x - x\partial_z), \quad L_z = -i(x\partial_y - y\partial_x).$$

The constant β represents the strength of short-range two-body interactions in the condensate with $\beta > 0$ corresponding to repulsive interaction and $\beta < 0$ to attractive interaction. The parameter λ characterizes the strength of the long-range DDI, and U_{dip} denotes the long-range DDI potential, defined as

$$U_{\text{dip}} = \frac{3}{4\pi|\mathbf{x}|^3}\left[1 - \frac{3(\mathbf{x}\cdot\mathbf{n})^2}{|\mathbf{x}|^2}\right] = \frac{3}{4\pi|\mathbf{x}|^3}\left[1 - 3\cos^2(\theta)\right], \quad \mathbf{x} \in \mathbb{R}^3. \tag{1.4}$$

Here, $\mathbf{n} = (n_1, n_2, n_3)^\top \in \mathbb{R}^3$ is a given unit vector, representing the dipole axis (or dipole moment), and θ is the angle between the dipole axis $\mathbf{n}$ and the vector $\mathbf{x}$. We consider that the dipoles are polarized along the z-axis by an external field, i.e., $\mathbf{n} = (0, 0, 1)^\top$. $V(\mathbf{x})$ is a given real-valued external trapping potential, determined by

the type of system under study. In most BEC experiments, a harmonic potential is employed to trap the condensate, i.e.,

$$V(\mathbf{x}) = \frac{1}{2}(\gamma_x x^2 + \gamma_y y^2 + \gamma_z z^2), \tag{1.5}$$

where γ_v $(v = x, y, z)$ is the trapping frequencies in the v-direction. The trapping frequencies can be very different in different directions, forming an anisotropic trap, such as those in disk-shaped and cigar-shaped condensates [5].

For BECs with rotation axis aligned along the z-axis, extensive mathematical and numerical studies on the dynamics have been conducted, and we direct readers to [4, 5, 6, 7, 8, 9, 12, 35, 13, 14, 18] for detailed information. On the numerical front, the time-splitting Fourier spectral method is widely used due to its stability, efficiency, and easy implementation, and it has been successfully adapted to dipolar and rotating BECs. The presence of the rotation term, giving the form of variable coefficients multiplied by the differential operator, introduces some difficulties. To overcome such difficulties, several successful techniques have been developed. For example, the rotation term is diagonalized automatically by employing special coordinate systems, such as polar/cylindrical coordinates [6, 7] or specific domains, such as disk domains [35]. In Cartesian coordinates, Bao et al. [9] applied the alternating direction implicit (ADI) technique to handle the angular momentum term and developed a second-order spectrally accurate method. In [8], a rotating Lagrangian coordinate (RLC) method was presented for rotating dipolar BEC, where the rotation term automatically vanishes. This facilitated the use of operator splitting methods or exponential integrators to develop high order schemes, such as exponential Runge-Kutta methods and Lawson methods [12].

However, one needs to switch back to the original Cartesian coordinates since physics experiments focus on the real-time dynamics in the rotating frame, i.e., the evolution of wave function ψ governed by the GPE (1.1)–(1.3). The coordinate transform is commonly implemented through Fourier spectral interpolation and its computation boils down to a summation of Fourier series at nonuniform grid. Naive direct summation requires $\mathcal{O}(N^{d+2})$ complexity, where N is grid points per spatial direction. Although the summation can be accelerated by the NonUniform Fast Fourier Transform (NUFFT) algorithm, which reduces the complexity to $CN^d \log(N)$, the prefactor C is super large. Therefore, the coordinate transform bottlenecks the simulation efficiency. To overcome this bottleneck, Liu et al. [23] proposed an efficient and accurate method based solely on FFT/iFFT pairs. Recently, Bernier et al. [10, 11] proposed the exact splitting method (ESM) for the Laplace-rotation-potential subproblem, but the splitting coefficients are obtained by solving a nonlinear system using an iterative method. Fortunately, Liu et al. [21] derived explicit formulas of coefficients for ESM in the *Laplace-rotation* subproblem by a simple block-by-block matrix matching. However, their work focused on the dynamics of rotating spin-1 BECs with rotation axis fixed along the z-axis, and the proposed scheme therein *cannot* be applied to an arbitrary-angle rotation case. It is worth emphasizing that the aforementioned methods all achieve spectral accuracy in the spatial direction.

While there are quite few studies on the development of numerical methods for dynamic simulation for dipolar BECs with arbitrary rotation axis. In this article, we aim to design high-order numerical schemes with high efficiency in the original Cartesian coordinates. To this end, there are two major challenges ahead.

The *first* challenge lies in the proper treatments of the rotation with arbitrary-angle (ArbRotation). The ADI technique can be adapted to this scenario by splitting

the angular momentum into three parts, and one can easily construct a second-order scheme (see (4.3) on page 51 in [26]). However, it is somewhat tedious to design high-order schemes. Recently, an orthogonal coordinate transformation method is proposed to simulate the arbitrary-angle rotating BECs without dipolar interactions [30], where they introduce a coordinate transformation to make the arbitrary-angle rotation aligned with the z-axis and apply the RLC method [8]. It is possible to construct high-order schemes, but the computational efficiency is not competitive when computing real-time dynamics because the coordinates' switch from orthogonal to Cartesian coordinates at every time step is time-consuming in simulation. In this paper, we aim to design an exact time splitting scheme with explicit splitting coefficients for the "*Laplace + arbitrary-angle rotation*" subproblem, which allows for an efficient implementation using purely FFT and easy adaptation to other relevant rotating systems. The ESM [10] is still applicable, but the coefficients are determined by a nonlinear system. Following the same ideas as shown in [21], we succeeded in deriving **explicit** formulas for coefficients by transforming the nonlinear system into linear equations through an elaborative block-by-block matrix matching. For example, for $\mathbf{\Omega} = (\omega_x, 0, 0)^\top$, the following splitting scheme holds true:

$$e^{i\tau[\Delta/2+\omega_x L_x]} = e^{-i\tau(\zeta_2 y^2+\zeta_3 z^2)} e^{-\tau\xi_3 z\partial_y} e^{i\tau\nabla^\top K\nabla} e^{-\tau\eta_3 y\partial_z} e^{-i\tau\mathbf{x}^\top P\mathbf{x}} \tag{1.6}$$

with suitable coefficients ζ_2, ζ_3, ξ_3, $\eta_3 \in \mathbb{R}$ and matrices K, $P \in \mathbb{R}^{3\times 3}$. Each suboperator can be accessed numerically efficiently, achieving spectral accuracy in phase space or exact computation in physical space. The resulting explicit coefficients makes the scheme (1.6) quite user-friendly and easy to implement.

The *second* challenge is the fast and accurate evaluation of 3D DDI (1.2). Lack of accuracy may cause spurious oscillations or significant loss of accuracy in the long-time dynamics. It is therefore imperative to develop an accurate and efficient DDI solver. Since the interaction kernel $U_{\rm dip}$ and its Fourier transform are both singular, it is crucial to handle these singularities properly to guarantee high accuracy. Over the past decades, several fast spectral methods based on the Fourier spectral method have been developed, including the NUFFT-based algorithm [19], Gaussian-Summation method (GauSum) [15], Kernel Truncation Method (KTM) [34], Anisotropic Truncated Kernel Method (ATKM) [16], and the newly developed far-field smooth approximation (FSA)-based method [24]. All these methods are spectrally accurate and efficient. Among them, the FSA-based method stands out as the optimal one because it ingeniously addresses the challenges of singularity, nonlocality, and anisotropy and achieves spectral accuracy with nearly optimal efficiency and minimum memory requirement. Therefore, we adopt the FSA-based method as the DDI solver in this article.

In this paper, we split the GPE (1.1) into a linear subproblem

$$i\partial_t\psi(\mathbf{x},t) = \left[-\frac{1}{2}\Delta - \mathbf{\Omega}\cdot\boldsymbol{L}\right]\psi(\mathbf{x},t) := \mathcal{H}_{\rm lin}\psi(\mathbf{x},t) \tag{1.7}$$

and a nonlinear subproblem

$$i\partial_t\psi(\mathbf{x},t) = \Big[V(\mathbf{x}) + \beta|\psi(\mathbf{x},t)|^2 + \lambda\Phi(\mathbf{x},t)\Big]\psi(\mathbf{x},t) := \mathcal{H}_{\rm non}\psi(\mathbf{x},t). \tag{1.8}$$

We derive an explicit and exact time integrator (2.3) for the Laplace-ArbRotation linear subproblem (1.7) and will refer to it hereafter as the Explicit-Exact-Integrator (**EEI**). In EEI, the wave function is approximated by the Fourier spectral method

and integrated exactly in the phase space. For the nonlinear subproblem (1.8), we can integrate it exactly in the physical space with an FSA-based solver for DDI evaluation. To sum up, each subproblem can be efficiently and exactly solved in either the physical or phase space, and it significantly simplifies the design of high-order time marching schemes. Hereafter, we refer to such splitting with only two operators as "compact" splitting.

This paper is organized as follows. In section 2, we propose an efficient and robust splitting Fourier spectral method to simulate the dynamics and prove that it is unconditionally stable. In section 3, we derive some dynamical laws for some physical quantities. Detailed spatial/temporal convergence tests for the DDI and wave function are presented in section 4, together with some interesting numerical results. Finally, some conclusions are drawn in section 5.

2. Numerical method. In the presence of a confining potential $V(\mathbf{x})$, the density $\rho = |\psi|^2$ is usually smooth and decays exponentially. This allows us to approximate ψ on a truncated regular domain rather than the whole space $\mathbb{R}^3$. For simplicity, we assume that ρ is compactly supported within a cubic domain $\mathbf{R}_L = [-L, L]^3$ and discretize the domain with N ($N \in 2\mathbb{Z}^+$) equally spaced grid points per spatial direction. Let $h = 2L/N$ denote the mesh size, with the physical index and uniform mesh grid set defined as

$$\mathcal{I}_N := \left\{ (j,k,\ell) \in \mathbb{Z}^3 \middle| \ -N/2 \le j,k,\ell \le N/2-1 \right\},$$
$$\mathcal{T}_N := \left\{ \mathbf{x}_{jk\ell} := (x_j, y_k, z_\ell)^\top := (jh, kh, \ell h)^\top, \quad (j,k,\ell) \in \mathcal{I}_N \right\}.$$

In our method, the Hamiltonian is split into two parts: the linear operator $\mathcal{H}_{\rm lin}$ (Laplace-ArbRotation terms) and the nonlinear operator $\mathcal{H}_{\rm non}$. Once the DDI is obtained, this splitting enables an exact, efficient, and simple evaluation of the nonlinear subproblem in physical space since the density ρ is conserved. To achieve this, the FSA-based method proves highly effective for 3D DDI calculation and offers spectral accuracy, nearly optimal efficiency, and minimum memory cost. For the linear subproblem, we construct an exact and explicit integrator (EEI). The key idea is to factorize the semigroup generated by Laplace-ArbRotation terms into a product of semigroups, each corresponding to a differential operator that can be efficiently computed. The details are provided in subsection 2.1.

To be exact, we denote the time sequence as $t_n = n\tau$ for $n = 0, 1, \ldots$ with a given time step $\tau > 0$. The solutions to the linear and nonlinear subproblems, starting from $t = t_n$, are expressed as $\psi(t) = e^{-i(t-t_n)\mathcal{H}_{\rm lin}}\psi^n$ and $\psi(t) = e^{-i(t-t_n)\mathcal{H}_{\rm non}}\psi^n$, respectively. High-order operator splitting schemes can be constructed as follows [36]:

$$\psi^{n+1} = \left[\prod_{j=1}^{m} e^{-ia_j\tau\mathcal{H}_{\rm lin}} e^{-ib_j\tau\mathcal{H}_{\rm non}} \right] \psi^n,$$

where $a_j, b_j \in \mathbb{C}$ are suitably chosen coefficients. For the second-order Strang splitting, we set $m = 2$, $a_1 = a_2 = \frac{1}{2}$ and $b_1 = 1$, $b_2 = 0$, while the fourth-order Yoshida scheme uses $m = 4$ with coefficients $a_1 = a_4 = \frac{1}{2(2-2^{1/3})}$, $a_2 = a_3 = \frac{1-2^{1/3}}{2(2-2^{1/3})}$, and $b_1 = b_3 = \frac{1}{2-2^{1/3}}$, $b_2 = -\frac{2^{1/3}}{2-2^{1/3}}$, $b_4 = 0$.

2.1. Exact temporal integrator for linear subproblem. The exact solution to the following linear problem:

$$\text{(2.1)}\qquad \begin{cases} i\partial_t\psi(\mathbf{x},t) = \left[-\frac{1}{2}\Delta - \boldsymbol{\Omega}\cdot\boldsymbol{L}\right]\psi(\mathbf{x},t), \quad t_n \le t \le t_{n+1}, \\ \psi(\mathbf{x},t_n) = \psi^n(\mathbf{x}), \quad \mathbf{x}\in\mathbf{R}_L \end{cases}$$

can be formally expressed as

$$\text{(2.2)}\qquad \psi(\mathbf{x},t) = e^{i(t-t_n)[\Delta/2+\boldsymbol{\Omega}\cdot\boldsymbol{L}]}\psi^n(\mathbf{x}).$$

The operator $e^{i\tau[\Delta/2+\boldsymbol{\Omega}\cdot\boldsymbol{L}]}$ cannot be directly accessed with both accuracy and efficiency. To address this, we factorize it into a product of seven suboperators exactly (see Theorem 4, p. 24 in [10] or Theorem 1, p. 14 in [11]), as shown below:

$$\text{(2.3)}\qquad \boxed{\begin{aligned} e^{i\tau[\Delta/2+\boldsymbol{\Omega}\cdot\boldsymbol{L}]} = {} & e^{-i\tau(\zeta_1x^2+\zeta_2y^2+\zeta_3z^2)}e^{-\tau(\xi_1y+\xi_2z)\partial_x}e^{-\tau\xi_3z\partial_y}e^{i\tau\nabla^\top K\nabla}e^{-\tau\eta_1x\partial_y} \\ & \times e^{-\tau(\eta_2x+\eta_3y)\partial_z}e^{-i\tau\mathbf{x}^\top P\mathbf{x}}, \end{aligned}}$$

with suitable coefficients ζ_1, ζ_2, ζ_3, ξ_1, ξ_2, ξ_3, $\eta_1,\eta_2,\eta_3\in\mathbb{R}$ and matrices K, $P\in\mathbb{R}^{3\times3}$. Clearly, each suboperator can be accessed numerically with great efficiency in either physical or phase space.

It appears unlikely that explicit expressions for such coefficients can be derived because doing so requires solving a nonlinear system that involves complicated matrix exponentials (see section 4.2 in [10]). In fact, such a nonlinear system can be turned into a series of linear equations through an elaborative block-by-block matrix matching. This observation allows us to successfully derive explicit and exact formulas for the coefficients, as presented in the following Theorem 1.

THEOREM 1. *The coefficients of exact splitting* (2.3) *for* $e^{i\tau[\Delta/2+\boldsymbol{\Omega}\cdot\boldsymbol{L}]}$ *are given explicitly by*

$$\text{(2.4)}\qquad \zeta_1 = \frac{(\omega_y^2+\omega_z^2)}{2f(\omega_x)}m, \qquad \xi_1 = \frac{g(-\omega_x,\omega_y,\omega_z)f(\omega_x)}{f(\omega_z)}, \qquad \eta_1 = -\frac{g(\omega_x,\omega_y,\omega_z)}{f(\omega_x)},$$

$$\text{(2.5)}\qquad \zeta_2 = \frac{(\omega_x^2-\omega_z^2)}{2f(\omega_z)}m, \qquad \xi_2 = -g(\omega_x,\omega_z,\omega_y)f(\omega_z), \qquad \eta_2 = \frac{g(\omega_x,\omega_z,\omega_y)}{f(\omega_z)},$$

$$\text{(2.6)}\qquad \zeta_3 = -\frac{1}{2}(\omega_x^2+\omega_y^2)m, \quad \xi_3 = \frac{g(\omega_z,\omega_y,\omega_x)f(\omega_z)}{f(\omega_x)}, \qquad \eta_3 = \frac{g(\omega_z,\omega_y,-\omega_x)}{f(\omega_z)},$$

$$\text{(2.7)}\qquad K = \frac{1}{2}(\Theta^{(2)}_{-\tau,\boldsymbol{\xi}})^\top\, W\, (\Theta^{(2)}_{\tau,\boldsymbol{\eta}})^\top, \qquad P = \frac{1}{2\tau^2}\left(W^\top\, \Theta^{(1)}_{\tau,\boldsymbol{\xi}}\, \Theta^{(2)}_{\tau,\boldsymbol{\eta}} - I_3\right),$$

where $m = \frac{1-\cos(|\boldsymbol{\Omega}|\tau)}{(|\boldsymbol{\Omega}|\tau)^2}$, $f(\omega_i) = \cos(|\boldsymbol{\Omega}|\tau) + \omega_i^2 m\tau^2$, $g(\omega_x,\omega_y,\omega_z) = \omega_x\omega_y m\tau + \omega_z\frac{\sin(|\boldsymbol{\Omega}|\tau)}{|\boldsymbol{\Omega}|\tau}$, $\boldsymbol{\xi} = (\xi_1,\xi_2,\xi_3)$, $\boldsymbol{\eta} = (\eta_1,\eta_2,\eta_3)$, $W = e^{\tau A}$ *with*

$$A = \begin{pmatrix} 0 & \omega_z & -\omega_y \\ -\omega_z & 0 & \omega_x \\ \omega_y & -\omega_x & 0 \end{pmatrix}, \quad \Theta^{(1)}_{\tau,\mathbf{v}} := \begin{pmatrix} 1 & \tau v_1 & \tau^2 v_1v_3 + \tau v_2 \\ 0 & 1 & \tau v_3 \\ 0 & 0 & 1 \end{pmatrix},$$

$$\Theta^{(2)}_{\tau,\mathbf{v}} := \begin{pmatrix} 1 & 0 & 0 \\ \tau v_1 & 1 & 0 \\ \tau v_2 & \tau v_3 & 1 \end{pmatrix}$$

with $\mathbf{v} = (v_1,v_2,v_3)$, *and* I_3 *is the* 3×3 *identity matrix.*

Proof. Using exact classical-quantum correspondence, the exact splitting of differential operators can be established through the exact splitting at the semigroup level generated by operators (see Proposition 4, p. 16 in [10]). We rewrite the exact operator splitting in (2.3) as

$$e^{-\tau p^w} = e^{-\tau p_1^w} e^{-\tau p_2^w} e^{-\tau p_3^w} e^{-\tau p_4^w} e^{-\tau p_5^w} e^{-\tau p_6^w} e^{-\tau p_7^w}, \tag{2.8}$$

where the Weyl quantization is defined as $p_m^w := \mathbf{z}^\top Q_m \mathbf{z}$ with $\mathbf{z} = (\mathbf{x}^\top, -i\nabla^\top)^\top$. Specifically,

$$p^w = -i(\Delta/2 + \boldsymbol{\Omega}\cdot\boldsymbol{L}) = \mathbf{z}^\top \frac{i}{2}\begin{pmatrix} 0 & A^\top \\ A & I_3 \end{pmatrix}\mathbf{z} := \mathbf{z}^\top Q\ \mathbf{z} \ \text{ with } \ A = \begin{pmatrix} 0 & \omega_z & -\omega_y \\ -\omega_z & 0 & \omega_x \\ \omega_y & -\omega_x & 0 \end{pmatrix},$$

$$p_1^w = i(\zeta_1 x^2 + \zeta_2 y^2 + \zeta_3 z^2) = \mathbf{z}^\top i\begin{pmatrix} D & 0 \\ 0 & 0 \end{pmatrix}\mathbf{z} := \mathbf{z}^\top Q_1\ \mathbf{z} \ \text{ with } \ D = \operatorname{diag}\{\zeta_1,\zeta_2,\zeta_3\},$$

$$p_2^w = (\xi_1 y + \xi_2 z)\partial_x = \mathbf{z}^\top \frac{i}{2}\begin{pmatrix} 0 & M_{\boldsymbol{\xi}}^\top \\ M_{\boldsymbol{\xi}} & 0 \end{pmatrix}\mathbf{z} := \mathbf{z}^\top Q_2\ \mathbf{z} \ \text{ with } \ M_{\boldsymbol{\xi}} = \begin{pmatrix} 0 & \xi_1 & \xi_2 \\ 0 & 0 & 0 \\ 0 & 0 & 0 \end{pmatrix},$$

$$p_3^w = \xi_3 z\partial_y = \mathbf{z}^\top \frac{i}{2}\begin{pmatrix} 0 & U_{\boldsymbol{\xi}}^\top \\ U_{\boldsymbol{\xi}} & 0 \end{pmatrix}\mathbf{z} := \mathbf{z}^\top Q_3\ \mathbf{z} \ \text{ with } \ U_{\boldsymbol{\xi}} = \begin{pmatrix} 0 & 0 & 0 \\ 0 & 0 & \xi_3 \\ 0 & 0 & 0 \end{pmatrix},$$

$$p_4^w = -i\nabla^\top K\nabla = \mathbf{z}^\top i\begin{pmatrix} 0 & 0 \\ 0 & K \end{pmatrix}\mathbf{z} := \mathbf{z}^\top Q_4\ \mathbf{z},$$

$$p_5^w = \eta_1 x\partial_y = \mathbf{z}^\top \frac{i}{2}\begin{pmatrix} 0 & M_{\boldsymbol{\eta}}^\top \\ M_{\boldsymbol{\eta}} & 0 \end{pmatrix}\mathbf{z} := \mathbf{z}^\top Q_5\ \mathbf{z} \ \text{ with } \ M_{\boldsymbol{\eta}} = \begin{pmatrix} 0 & 0 & 0 \\ \eta_1 & 0 & 0 \\ 0 & 0 & 0 \end{pmatrix},$$

$$p_6^w = (\eta_2 x + \eta_3 y)\partial_z = \mathbf{z}^\top \frac{i}{2}\begin{pmatrix} 0 & U_{\boldsymbol{\eta}}^\top \\ U_{\boldsymbol{\eta}} & 0 \end{pmatrix}\mathbf{z} := \mathbf{z}^\top Q_6\ \mathbf{z} \ \text{ with } \ U_{\boldsymbol{\eta}} = \begin{pmatrix} 0 & 0 & 0 \\ 0 & 0 & 0 \\ \eta_2 & \eta_3 & 0 \end{pmatrix},$$

$$p_7^w = i\mathbf{x}^\top P\mathbf{x} = \mathbf{z}^\top i\begin{pmatrix} P & 0 \\ 0 & 0 \end{pmatrix}\mathbf{z} := \mathbf{z}^\top Q_7\ \mathbf{z}.$$

Then, we only need to focus on

$$e^{-2i\tau J_6 Q} = e^{-2i\tau J_6 Q_1} e^{-2i\tau J_6 Q_2} e^{-2i\tau J_6 Q_3} e^{-2i\tau J_6 Q_4} e^{-2i\tau J_6 Q_5} e^{-2i\tau J_6 Q_6} e^{-2i\tau J_6 Q_7}, \tag{2.9}$$

where J_6 denotes the fundamental symplectic matrix given by $J_6 := \left(\begin{smallmatrix} 0 & I_3 \\ -I_3 & 0 \end{smallmatrix}\right)$. Using the definition of the matrix exponential, we evaluate (2.9) explicitly term by term and derive

$$\begin{pmatrix} e^{\tau A} & \tau e^{\tau A} \\ 0 & e^{\tau A} \end{pmatrix} = \begin{pmatrix} I_3 & 0 \\ -2\tau D & I_3 \end{pmatrix}\begin{pmatrix} \Theta^{(1)}_{\tau,\boldsymbol{\xi}} & 0 \\ 0 & \Theta^{(2)}_{-\tau,\boldsymbol{\xi}} \end{pmatrix}\begin{pmatrix} I_3 & 2\tau K \\ 0 & I_3 \end{pmatrix}\begin{pmatrix} \Theta^{(2)}_{\tau,\boldsymbol{\eta}} & 0 \\ 0 & \Theta^{(1)}_{-\tau,\boldsymbol{\eta}} \end{pmatrix} \times \begin{pmatrix} I_3 & 0 \\ -2\tau P & I_3 \end{pmatrix} \tag{2.10}$$

$$= \begin{pmatrix} \Theta^{(1)}_{\tau,\boldsymbol{\xi}}\Theta^{(2)}_{\tau,\boldsymbol{\eta}} - 2\tau G_{12}P & 2\tau\Theta^{(1)}_{\tau,\boldsymbol{\xi}}K\Theta^{(1)}_{-\tau,\boldsymbol{\eta}} \\ -2\tau D\Theta^{(1)}_{\tau,\boldsymbol{\xi}}\Theta^{(2)}_{\tau,\boldsymbol{\eta}} - 2\tau G_{22}P & -2\tau DG_{12} + \Theta^{(2)}_{-\tau,\boldsymbol{\xi}}\Theta^{(1)}_{-\tau,\boldsymbol{\eta}} \end{pmatrix}$$
$$:= \begin{pmatrix} G_{11} & G_{12} \\ G_{21} & G_{22} \end{pmatrix},$$

where the second matrix on the right-hand side of (2.10) is $e^{-2i\tau J_6 Q_2}e^{-2i\tau J_6 Q_3}$, and the fourth matrix corresponds to $e^{-2i\tau J_6 Q_5}e^{-2i\tau J_6 Q_6}$. At first glance, the above equations seem like a complicated **nonlinear** system. In fact, we can derive exact and explicit formulas for these coefficients by solving a **linear** system through an elaborative block-by-block matching process. Starting from the relation $G_{22} = e^{\tau A}$, we sequentially compute ζ_1, η_1, ζ_2, ξ_1, η_3, η_2, ξ_2, ξ_3, and ζ_3 by solving linear equations. Next, we compute K and P directly via matrix inversion using $G_{11} = e^{\tau A}$ and $G_{12} = \tau e^{\tau A}$. Finally, we verify that $G_{21} = 0$ for the derived coefficients.

To be specific, a calculation shows that

$$e^{\tau A} = \begin{pmatrix} f(\omega_x) & g(\omega_x,\omega_y,\omega_z)\tau & g(\omega_x,\omega_z,-\omega_y)\tau \\ g(\omega_x,\omega_y,-\omega_z)\tau & f(\omega_y) & g(\omega_z,\omega_y,\omega_x)\tau \\ g(\omega_x,\omega_z,\omega_y)\tau & g(\omega_z,\omega_y,-\omega_x)\tau & f(\omega_z) \end{pmatrix} := W = (u_{ij})_{3\times 3}. \tag{2.11}$$

Using $G_{22} = -2\tau DG_{12} + \Theta^{(2)}_{-\tau,\boldsymbol{\xi}}\Theta^{(1)}_{-\tau,\boldsymbol{\eta}} = W$, we have $(I_3 + 2\tau^2 D)W = \Theta^{(2)}_{-\tau,\boldsymbol{\xi}}\Theta^{(1)}_{-\tau,\boldsymbol{\eta}}$, that is,

$$\begin{cases} (1+2\tau^2\zeta_1)u_{11} = 1, \quad (1+2\tau^2\zeta_1)u_{12} = -\tau\eta_1, \\ (1+2\tau^2\zeta_2)u_{21} = -\tau\xi_1, \quad (1+2\tau^2\zeta_2)u_{22} = \tau^2\xi_1\eta_1 + 1, \\ (1+2\tau^2\zeta_1)u_{13} = -\tau\eta_2 + \tau^2\eta_1\eta_3, \quad (1+2\tau^2\zeta_2)u_{23} = -\tau\xi_1(-\tau\eta_2 + \tau^2\eta_1\eta_3) - \tau\eta_3, \\ (1+2\tau^2\zeta_3)u_{31} = -\tau\xi_2, \quad (1+2\tau^2\zeta_3)u_{32} = \tau^2\eta_1\xi_2 - \tau\xi_3, \\ (1+2\tau^2\zeta_3)u_{33} = -\tau\xi_2(-\tau\eta_2 + \tau^2\eta_1\eta_3) + \tau^2\xi_3\eta_3 + 1. \end{cases}$$

Solving the above equations, we derive the formulas for ζ_1, ζ_2, ζ_3, ξ_1, ξ_2, ξ_3, η_1, η_2, and η_3, as shown in Eqns. (2.4)–(2.6). Then, using the following relations

$$G_{12} = 2\tau\Theta^{(1)}_{\tau,\boldsymbol{\xi}}K\Theta_{-\tau,\boldsymbol{\eta}} = \tau W, \quad G_{11} = \Theta_{\tau,\boldsymbol{\xi}}\Theta^{\top}_{\tau,\eta} - 2\tau G_{12}P = W,$$

we obtain

$$K = \frac{1}{2}\big(\Theta^{(1)}_{\tau,\boldsymbol{\xi}}\big)^{-1}\, W\, \big(\Theta^{(1)}_{-\tau,\boldsymbol{\eta}}\big)^{-1} = \frac{1}{2}\big(\Theta^{(2)}_{-\tau,\boldsymbol{\xi}}\big)^{\top}\, W\, \big(\Theta^{(2)}_{\tau,\boldsymbol{\eta}}\big)^{\top},$$
$$P = \frac{1}{2\tau^2}W^{-1}\left(\Theta^{(1)}_{\tau,\boldsymbol{\xi}}\,\Theta^{(2)}_{\tau,\boldsymbol{\eta}} - W\right) = \frac{1}{2\tau^2}\left(W^{\top}\,\Theta^{(1)}_{\tau,\boldsymbol{\xi}}\,\Theta^{(2)}_{\tau,\boldsymbol{\eta}} - I_3\right).$$

In the following, we verify $G_{21} = 0$ under the above derived coefficients for a consistency check. Specifically, the relation

$$(2\tau^2 D + I_3)W = \Theta^{(2)}_{-\tau,\boldsymbol{\xi}}\Theta^{(1)}_{-\tau,\boldsymbol{\eta}}$$

holds true. Then, it follows that

$$W^{\top} = W^{-1} = (\Theta^{(1)}_{-\tau,\boldsymbol{\eta}})^{-1}(\Theta^{(2)}_{-\tau,\boldsymbol{\xi}})^{-1}(2\tau^2 D + I_3).$$

Taking the transpose of both sides and using the relations $(\Theta^{(1)}_{-\tau,\boldsymbol{\eta}})^{-\top} = \Theta^{(2)}_{\tau,\boldsymbol{\eta}}$ and $(\Theta^{(2)}_{-\tau,\boldsymbol{\xi}})^{-\top} = \Theta^{(1)}_{\tau,\boldsymbol{\xi}}$, we obtain

$$W = (2\tau^2 D + I_3)^{\top} (\Theta^{(2)}_{-\tau,\boldsymbol{\xi}})^{-\top} (\Theta^{(1)}_{-\tau,\boldsymbol{\eta}})^{-\top} = (2\tau^2 D + I_3)\ \Theta^{(1)}_{\tau,\boldsymbol{\xi}}\ \Theta^{(2)}_{\tau,\boldsymbol{\eta}}.$$

This implies that

$$\begin{aligned} G_{21} &= -2\tau D \Theta^{(1)}_{\tau,\boldsymbol{\xi}} \Theta^{(2)}_{\tau,\boldsymbol{\eta}} - 2\tau W \left[\frac{1}{2\tau^2} \left(W^{\top} \Theta^{(1)}_{\tau,\boldsymbol{\xi}} \Theta^{(2)}_{\tau,\boldsymbol{\eta}} - I_3 \right) \right] \\ &= -\frac{1}{\tau} (2\tau^2 D + I_3) \Theta^{(1)}_{\tau,\boldsymbol{\xi}} \Theta^{(2)}_{\tau,\boldsymbol{\eta}} + \frac{1}{\tau} W = -\frac{1}{\tau} W + \frac{1}{\tau} W = 0. \end{aligned}$$

Proof is completed. ∎

The suboperators in (2.3) are well approximated using the Fourier spectral method with great efficiency because of FFT/iFFT pairs [29]. Specifically, the spectral approximations of wave function ψ in the α-direction ($\alpha = x, y, z$) are given as follows:

$$\begin{aligned} \psi(x,y,z) &\approx \sum_{p=-N/2}^{N/2-1} (\widehat{\psi}_{yz})_p\ e^{i\nu_p^x x}, \quad (\widehat{\psi}_{yz})_p = \frac{1}{N} \sum_{j=-N/2}^{N/2-1} \psi(x_j,y,z)\ e^{-i\nu_p^x x_j}, \\ \psi(x,y,z) &\approx \sum_{q=-N/2}^{N/2-1} (\widehat{\psi}_{xz})_q\ e^{i\nu_q^y y}, \quad (\widehat{\psi}_{xz})_q = \frac{1}{N} \sum_{k=-N/2}^{N/2-1} \psi(x,y_k,z)\ e^{-i\nu_q^y y_k}, \\ \psi(x,y,z) &\approx \sum_{s=-N/2}^{N/2-1} (\widehat{\psi}_{xy})_s\ e^{i\nu_s^z z}, \quad (\widehat{\psi}_{xy})_s = \frac{1}{N} \sum_{\ell=-N/2}^{N/2-1} \psi(x,y,z_\ell)\ e^{-i\nu_s^z z_\ell}, \end{aligned}$$

where $\nu_p^x = (2\pi p)/(2L)$, $\nu_q^y = (2\pi q)/(2L)$ and $\nu_s^z = (2\pi s)/(2L)$. The scheme (2.3) is then discretized as follows:

$$\begin{aligned}
&\psi^{(1)}_{jk\ell} = e^{-i\tau \mathbf{x}_{jk\ell}^{\top} P \mathbf{x}_{jk\ell}}\ \psi^{n}_{jk\ell} && (x,y,z)\text{-physical}, \\
&\psi^{(2)}_{jks} = e^{-i\tau(\eta_2 x_j + \eta_3 y_k)\nu_s^z}\ \widehat{(\psi^{(1)}_{jk})}_s && (x,y)\text{-physical}, z\text{-phase}, \\
&\psi^{(3)}_{jqs} = e^{-i\tau\eta_1 x_j \nu_q^y}\ \widehat{(\psi^{(2)}_{js})}_q && x\text{-physical}, (y,z)\text{-phase}, \\
&\psi^{(4)}_{pqs} = e^{-i\tau \boldsymbol{\nu}_{pqs}^{\top} K \boldsymbol{\nu}_{pqs}}\ \widehat{(\psi^{(3)}_{qs})}_p && (x,y,z)\text{-phase}, \\
&\psi^{(5)}_{pq\ell} = \sum_{s\in\mathcal{J}} \psi^{(4)}_{pqs}\ e^{i\nu_s^z z_\ell} && z\text{-physical}, (x,y)\text{-phase}, \\
&\psi^{(6)}_{pk\ell} = \sum_{q\in\mathcal{J}} e^{-i\tau\xi_3 z_\ell \nu_q^y}\ \psi^{(5)}_{pq\ell}\ e^{i\nu_q^y y_k} && (y,z)\text{-physical}, x\text{-phase}, \\
&\psi^{(7)}_{jk\ell} = \sum_{p\in\mathcal{J}} e^{-i\tau(\xi_1 y_k + \xi_2 z_\ell)\nu_p^x}\ \psi^{(6)}_{pk\ell}\ e^{i\nu_p^x x_j} && (x,y,z)\text{-physical}, \\
&\psi^{n+1}_{jk\ell} = e^{-i\tau(\zeta_1 x_j^2 + \zeta_2 y_k^2 + \zeta_3 z_\ell^2)}\ \psi^{(7)}_{jk\ell} && (x,y,z)\text{-physical}.
\end{aligned} \tag{2.12}$$

where $\boldsymbol{\nu}_{pqs} = (\nu_p^x, \nu_q^y, \nu_s^z)^{\top}$, $\mathcal{J} = \{-N/2, \ldots, N/2-1\}$, and $\psi^n_{jk\ell}$ denote the numerical approximation of $\psi(x_j, y_k, z_\ell, t_n)$ for $(j,k,\ell) \in \mathcal{I}_N$.

Remark 2.1 (**Efficiency**). The coefficients $\zeta_1, \zeta_2, \zeta_3, \xi_1, \xi_2, \xi_3, \eta_1, \eta_2, \eta_3, K$, and P depend solely on the angular velocity vector $\boldsymbol{\Omega}$ and the time step τ. Once these parameters are determined, the coefficients can be calculated once for all in the precomputation step. For the computational costs, (2.12) needs $\mathbf{3N^2}$ pairs of **one-dimensional** FFT and iFFT, and the complexity is $\mathcal{O}(N^3 \log(N))$.

Remark 2.2. In the special case where the rotation axis is aligned with the polarization axis (z-axis), i.e., $\omega_x = \omega_y = 0$, our method for the *Laplace-ArbRotation* subproblem aligns with the scheme introduced in [21].

2.2. Exact computation of nonlinear subproblem with FSA for DDI. In this subsection, we introduce an exact solution to the following nonlinear subproblem

$$\begin{cases} i\partial_t\psi(\mathbf{x},t) = \left[V(\mathbf{x}) + \beta|\psi|^2 + \lambda\Phi\right]\psi(\mathbf{x},t), \quad t_n \le t \le t_{n+1}, \\ \psi(\mathbf{x},t_n) = \psi^n(\mathbf{x}), \quad \mathbf{x}\in\mathbf{R}_L. \end{cases} \tag{2.13}$$

We demonstrate that the density $\rho = |\psi|^2$ is time-invariant, that is, $\rho(\mathbf{x},t) \equiv \rho(\mathbf{x},t_n) := \rho^n$ for any time $t \in [t_n, t_{n+1}]$. It can be proved by multiplying (1.1) by $\bar{\psi}$ and taking the imaginary part, i.e., $\partial_t\rho = (\partial_t\psi)\bar{\psi} + \psi(\partial_t\bar{\psi}) = 2\,\mathrm{Im}[(i\partial_t\psi)\bar{\psi}] = 0$. Therefore, $\Phi(\mathbf{x},t) \equiv \Phi(\mathbf{x},t_n) = [U_{\mathrm{dip}} * \rho^n](\mathbf{x}) := \Phi^n$ for $t \in [t_n, t_{n+1}]$. Clearly, the nonlinear ODE (2.13) becomes a linear one, and the exact solution reads as follows:

$$\psi(\mathbf{x},t) = e^{-i(t-t_n)\left[V(\mathbf{x})+\beta|\psi^n|^2+\lambda\Phi^n\right]}\psi^n(\mathbf{x}). \tag{2.14}$$

The primary challenge lies in achieving an accurate and efficient computation of the DDI $\Phi(\mathbf{x})$. In fact, the DDI can be reformulated as

$$\Phi(\mathbf{x}) = [U_{\mathrm{dip}} * \rho](\mathbf{x}) = -\rho(\mathbf{x}) - 3\left[\frac{1}{4\pi|\mathbf{x}|} * \partial_{\mathbf{nn}}\rho\right](\mathbf{x}) := -\rho(\mathbf{x}) - 3[U * \rho_1](\mathbf{x}),$$

where $\partial_{\mathbf{n}} = \mathbf{n}\cdot\nabla$, $\partial_{\mathbf{nn}} = \partial_{\mathbf{n}}(\partial_{\mathbf{n}})$, and the 3D Coulomb kernel reads as $U(\mathbf{x}) := \frac{1}{4\pi|\mathbf{x}|}$. Therefore, the DDI can be computed via the 3D Coulomb potential with the source term $\rho_1 := \partial_{\mathbf{nn}}\rho$, where the function ρ_1 can be readily obtained using the Fourier spectral method (see section 2 in [29]).

The FSA-based method proves highly effective for the nonlocal potential calculation and offers spectral accuracy, nearly optimal efficiency, and minimum memory cost [24]. The basic idea is to split the potential into a regular integral and a singular integral using the 3D Coulomb kernel's far-field smooth approximation

$$U^\varepsilon(r) := U(r)\,\mathrm{Erf}\left(\frac{r}{\varepsilon}\right) = \frac{1}{4\pi r}\,\mathrm{Erf}\left(\frac{r}{\varepsilon}\right), \tag{2.15}$$

where $\mathrm{Erf}(x) = \frac{2}{\sqrt{\pi}}\int_0^x e^{-t^2}\mathrm{d}t$ is the error function, and ε is a positive parameter that will be chosen later. The far-field smooth approximation (FSA) function U^ε satisfies the following two properties:

(2.16)

(a) $U^\varepsilon(\mathbf{x})$ is *smooth* and *radially symmetric*,
(b) $\displaystyle\int_{R_0}^{\infty} \lvert(U-U^\varepsilon)(r)\rvert r^{d-1}\mathrm{d}r \le \varepsilon_{\mathrm{tol}}$, where $\varepsilon_{\mathrm{tol}} \ll 1$ is the desired resolution,

where $R_0 = 2L$.

To be precise, we have

$$\begin{aligned} \Phi_1(\mathbf{x}) &:= \int_{\mathbb{R}^d} U(\mathbf{x}-\mathbf{y})\rho_1(\mathbf{y})\mathrm{d}\mathbf{y} \\ &= \int_{\mathbb{R}^d} U^\varepsilon(\mathbf{x}-\mathbf{y})\rho_1(\mathbf{y})\mathrm{d}\mathbf{y} + \int_{\mathbb{R}^d} (U-U^\varepsilon)(\mathbf{x}-\mathbf{y})\rho_1(\mathbf{y})\mathrm{d}\mathbf{y} \\ &:= \Phi_1^{\mathrm{R}}(\mathbf{x}) + \Phi_1^{\mathrm{S}}(\mathbf{x}). \end{aligned} \tag{2.17}$$

The regular integral is well resolved using the trapezoidal rule. For the singular integral, we approximate the density ρ_1 on a bounded domain by a Fourier spectral method following the same way as the ATKM [16]. Fortunately, due to the second property of (2.16), the required bounded domain Fourier transform of $(U-U^\varepsilon)$ can be well approximated by the whole space Fourier transform, which has an analytical explicit formula, thus waiving the requirement of a technically complicated quadrature.

For the evaluation of the regular integral $\Phi_1^{\mathrm{R}}(\mathbf{x})$, using the compact support of density and applying the trapezoidal rule, we obtain

$$\begin{aligned}\Phi_1^{\mathrm{R}}(x_j,y_k,z_\ell) &\approx h^3 \sum_{(j',k',\ell')\in\mathcal{I}_N} U^\varepsilon\big((j-j')h,(k-k')h,(\ell-\ell')h\big)\ \rho_1(x_{j'},y_{k'},z_{\ell'})\\ &:= \sum_{(j',k',\ell')\in\mathcal{I}_N} T^{(1)}_{j-j',k-k',\ell-\ell'}\ \rho_{1,j',k',\ell'}, \end{aligned} \tag{2.18}$$

where $\rho_{1,j',k',\ell'} := \rho_1(x_{j'},y_{k'},z_{\ell'})$ and the tensor $T^{(1)}_{j,k,\ell}$ is given explicitly as

$$T^{(1)}_{j,k,\ell} = h^3\ U^\varepsilon(jh,kh,\ell h).$$

For the evaluation of the singular integral $\Phi_1^{\mathrm{S}}(\mathbf{x})$, using the fact that the density is compactly supported in $\mathbf{R}_L$, we have

$$\Phi_1^{\mathrm{S}}(\mathbf{x}) \approx \int_{\mathbf{R}_L} (U-U^\varepsilon)(\mathbf{x}-\mathbf{y})\rho_1(\mathbf{y})\mathrm{d}\mathbf{y} = \int_{\mathbf{R}_{2L}} (U-U^\varepsilon)(\mathbf{y})\rho_1(\mathbf{x}-\mathbf{y})\mathrm{d}\mathbf{y}. \tag{2.19}$$

To integrate (2.19), one requires obtaining a good approximation of $\rho_1(\mathbf{x})$ over $\mathbf{R}_{3L}$. A natural way is to first zero-pad the density from $\mathbf{R}_L$ to $\mathbf{R}_{3L}$ and then construct a Fourier series approximation therein. In fact, a two-fold zero-padding to $\mathbf{R}_{2L}$ is sufficient to guarantee spectral accuracy with the help of the periodicity of the Fourier basis [15, 22]. To be specific, the approximation reads as

$$(\rho_1)_N(\mathbf{z}) := \sum_{\boldsymbol{\nu}\in\Lambda} (\widetilde{\rho_1})_{\boldsymbol{\nu}}\ e^{i\boldsymbol{\nu}\cdot\mathbf{z}}, \quad \mathbf{z}\in\mathbf{R}_{2L}, \tag{2.20}$$

where $\Lambda := \{\boldsymbol{\nu} := (\nu_p,\nu_q,\nu_s) = \frac{\pi}{2L}(p,q,s) \in \frac{\pi}{2L}\mathbb{Z}^d \ \big|(p,q,s)\in\mathcal{I}_{2N}\}$ denotes the Fourier mesh grid, and the Fourier coefficients read as

$$(\widetilde{\rho_1})_{\boldsymbol{\nu}} = \frac{1}{(2N)^3} \sum_{\mathbf{z_p}\in\mathcal{T}_{2N}} \rho_1(\mathbf{z_p}) e^{-i\boldsymbol{\nu}\cdot\mathbf{z_p}}, \quad \boldsymbol{\nu}\in\Lambda. \tag{2.21}$$

By substituting $(\rho_1)_N$ for ρ_1 in (2.19), we have

$$\begin{aligned}\Phi_1^{\mathrm{S}}(\mathbf{x}) &\approx \int_{\mathbf{R}_{2L}} (U-U^\varepsilon)(\mathbf{y})(\rho_1)_N(\mathbf{x}-\mathbf{y})\mathrm{d}\mathbf{y} \\ &= \sum_{\boldsymbol{\nu}\in\Lambda} \left[\int_{\mathbf{R}_{2L}} (U-U^\varepsilon)(\mathbf{y}) e^{-i\boldsymbol{\nu}\cdot\mathbf{y}}\mathrm{d}\mathbf{y}\right]\ (\widetilde{\rho_1})_{\boldsymbol{\nu}}\ e^{i\boldsymbol{\nu}\cdot\mathbf{x}} \end{aligned} \tag{2.22}$$

$$:= \sum_{\boldsymbol{\nu}\in\Lambda} W(\boldsymbol{\nu})\ (\widetilde{\rho_1})_{\boldsymbol{\nu}}\ e^{i\boldsymbol{\nu}\cdot\mathbf{x}}, \quad \mathbf{x}\in\mathbf{R}_L, \tag{2.23}$$

where $W(\boldsymbol{\nu})$ is the Fourier transform of $(U-U^\varepsilon)$ over $\mathbf{R}_{2L}$, i.e.,

$$W(\boldsymbol{\nu}) = \int_{\mathbf{R}_{2L}} (U-U^\varepsilon)(\mathbf{y}) e^{-i\boldsymbol{\nu}\cdot\mathbf{y}}\mathrm{d}\mathbf{y}. \tag{2.24}$$

Unfortunately, the above bounded domain Fourier transform lacks explicit analytical expressions. Therefore, one has to develop suitable numerical quadratures. For instance, Greengard et al. [16] proposed an efficient and accurate quadrature based on the Gaussian-sum approximation. In fact, we can approximate $W(\boldsymbol{\nu})$ by the Fourier transform of $(U-U^\varepsilon)$ on the whole space using the second property of (2.16). That is,

$$W(\boldsymbol{\nu}) \approx \int_{\mathbb{R}^d} (U-U^\varepsilon)(\mathbf{y})\ e^{-i\boldsymbol{\nu}\cdot\mathbf{y}} \mathrm{d}\ \mathbf{y}. \tag{2.25}$$

By choosing an appropriate parameter ε, we can control the approximation error as small as any desired precision. The above whole space integral is well-defined because $(U-U^\varepsilon) \in L^1(\mathbb{R}^3)$. The Fourier transform of $(U-U^\varepsilon)$ is radially symmetric [34] and is explicitly given as follows:

$$\widehat{(U-U^\varepsilon)}(\boldsymbol{\nu}) = 4\pi \int_0^\infty (U-U^\varepsilon)(r)\ \frac{\sin(|\boldsymbol{\nu}|r)}{|\boldsymbol{\nu}|r}\ r^2\ \mathrm{d}r = \frac{1}{|\boldsymbol{\nu}|^2}\left[1-e^{-\frac{1}{4}|\boldsymbol{\nu}|^2\varepsilon^2}\right]. \tag{2.26}$$

Remark 2.3 (Parameter choice of ε). The parameter ε is selected to satisfy condition (b) of (2.16). Roughly speaking, $\varepsilon < R_0/5.85$ achieves about 16 digits of accuracy.

The quadrature (2.23) can be reformulated as a discrete convolution structure by plugging (2.21) into (2.23) and switching the summation order, that is,

(2.27)

$$\begin{aligned}
&\Phi_1^{\mathrm{S}}(x_j, y_k, z_\ell) \\
&\quad = \sum_{(p,q,s)\in\mathcal{I}_{2N}} W(\boldsymbol{\nu}_{pqs})(\widetilde{\rho}_1)_{\boldsymbol{\nu}_{pqs}}\ e^{\frac{2\pi i}{2N}(pj+qk+s\ell)} \\
&\quad = \sum_{(j',k',\ell')\in\mathcal{I}_N} \left[\frac{1}{(2N)^3} \sum_{(p,q,s)\in\mathcal{I}_{2N}} W(\boldsymbol{\nu}_{pqs})\ e^{\frac{2\pi i}{2N}\left[p(j-j')+q(k-k')+s(\ell-\ell')\right]}\right] \rho_{1,j',k',\ell'} \\
&\quad := \sum_{(j',k',\ell')\in\mathcal{I}_N} T^{(2)}_{j-j',k-k',\ell-\ell'}\ \rho_{1,j',k',\ell'}.
\end{aligned}$$

The tensor is actually the inverse discrete Fourier transform of vector $\{W(\mathbf{k})\}_{\mathbf{k}\in\Lambda} \in \mathbb{C}^{(2N)^3}$, and it can be computed *once for all* within $\mathcal{O}(9N^3\log(9N^3))$ float operations using iFFT.

To sum up, the quadratures of both parts can be rewritten as discrete convolutions (i.e., (2.18) and (2.27)). Then, our method can be simplified to a single discrete convolution as follows:

$$(\Phi_1)_N(x_j, y_k, z_\ell) := \sum_{(j',k',\ell')\in\mathcal{I}_N} T_{j-j',k-k',\ell-\ell'}\ \rho_{1,j',k',\ell'}, \tag{2.28}$$

where $T_{j,k,\ell} = T^{(1)}_{j,k,\ell} + T^{(2)}_{j,k,\ell}$.

The tensor generation process is efficient and easy to implement. Once the tensor is generated, the discrete convolution (2.28) can be implemented using only FFT/iFFT operators and pointwise multiplications on vectors of length $(2N)^3$. For further details, we refer the reader to [22, 34].

Remark 2.4. The above discussion can be easily adapted to the anisotropic case with minor modifications. For detailed information, see section 2.4 in [24].

Remark 2.5 (Different dipole orientations). When the two dipoles are not polarized along the same axis, the kernel is given by

$$U_{\mathrm{dip}}(\mathbf{x}) = \frac{3}{4\pi}\frac{\mathbf{m}\cdot\mathbf{n} - 3(\mathbf{x}\cdot\mathbf{m})(\mathbf{x}\cdot\mathbf{n})/|\mathbf{x}|^2}{|\mathbf{x}|^3},$$

where $\mathbf{n}$ and $\mathbf{m} \in \mathbb{R}^3$ are unit vectors representing the dipole orientations [19]. The corresponding 3D DDI is reformulated as

$$\Phi(\mathbf{x}) = -(\mathbf{m}\cdot\mathbf{n})\rho(\mathbf{x}) - 3\frac{1}{4\pi|\mathbf{x}|} * (\partial_{\mathbf{nm}}\rho),$$

where $\partial_{\mathbf{m}} = \mathbf{m}\cdot\nabla$ and $\partial_{\mathbf{nm}} = \partial_{\mathbf{n}}(\partial_{\mathbf{m}})$. In fact, the DDI can be computed via the 3D Coulomb potential with the source term $\rho_1 := \partial_{\mathbf{nm}}\rho$, where the function ρ_1 can be obtained using the Fourier spectral method. Therefore, our method can also be extended to this case with ease, and the results of the accuracy test are presented in Table 3.

2.3. Numerical stability. In this subsection, we prove that our method is unconditionally stable, which implies that the mass conservation holds at a discrete level. To this end, we define the discrete l^2-norm of ψ^n as $\|\psi^n\|_{l^2} = (h^3\sum_{(j,k,\ell)\in\mathcal{I}_N}|\psi^n_{jk\ell}|^2)^{\frac{1}{2}}$.

LEMMA 1 (**Numerical stability**). *The compact splitting Fourier spectral method is unconditionally stable, i.e., for any h and τ, we obtain*

$$\|\psi^n\|_{l^2}^2 = \|\psi^0\|_{l^2}^2.$$

In other words, the mass is conserved at discrete level.

Proof. For the nonlinear subproblem (2.14), it is clear that

$$\|\psi^{n+1}\|_{l^2}^2 = \|e^{-i\tau\left[V+\beta|\psi^n|^2+\lambda\Phi^n\right]}\psi^n\|_{l^2}^2 = \|\psi^n\|_{l^2}^2.$$

While for the linear subproblem (2.12), we have

$$\|\psi^{(1)}\|_{l^2}^2 = h^3\sum_{(j,k,\ell)\in\mathcal{I}_N}|e^{-i\tau\mathbf{x}_{jk\ell}^\top P\mathbf{x}_{jk\ell}}\psi^n_{jk\ell}|^2 = \|\psi^n\|_{l^2}^2.$$

Using the following identities:

$$\sum_{s=-N/2}^{N/2-1} e^{\frac{2\pi i\ell s}{N}} = \begin{cases} 0, & \ell \neq mN, \\ N, & \ell = mN, \end{cases} \qquad m\in\mathbb{Z},$$

we obtain

$$\begin{aligned}\sum_{(j,k,s)\in\mathcal{I}_N}|\psi^{(2)}_{jks}|^2 &= \sum_{(j,k,s)\in\mathcal{I}_N}\left|e^{-i\tau(\eta_2x_j+\eta_3y_k)\nu_s^z}\,\widehat{(\psi^{(1)}_{jk})}_s\right|^2 \\ &= \frac{1}{N^2}\sum_{(j,k,s)\in\mathcal{I}_N}\left|\sum_{\ell=-N/2}^{N/2-1}\psi^{(1)}_{jk\ell}\,e^{\frac{2\pi i\ell s}{N}}\right|^2 = \frac{1}{N}\sum_{(j,k,\ell)\in\mathcal{I}_N}|\psi^{(1)}_{jk\ell}|^2.\end{aligned}$$

Similarly, we have

$$\begin{aligned}\|\psi^{(7)}\|_{l^2}^2 &= h^3\sum_{(j,k,\ell)\in\mathcal{I}_N}|\psi^{(7)}_{jk\ell}|^2 = h^3N^3\sum_{(p,q,s)\in\mathcal{I}_N}|\widehat{(\psi^{(3)}_{qs})}_p|^2 = h^3N^2\sum_{(j,q,s)\in\mathcal{I}_N}|\psi^{(3)}_{jqs}|^2 \\ &= h^3N\sum_{(j,k,s)\in\mathcal{I}_N}|\psi^{(2)}_{jks}|^2 = h^3\sum_{(j,k,\ell)\in\mathcal{I}_N}|\psi^{(1)}_{jk\ell}|^2 = \|\psi^{(1)}\|_{l^2}^2.\end{aligned}$$

To sum up, we can prove that the following relation

$$\|\psi^{n+1}\|_{l^2}^2 = \|\psi^{(7)}\|_{l^2}^2 = \|\psi^{(1)}\|_{l^2}^2 = \|\psi^n\|_{l^2}^2$$

holds true. ∎

3. Dynamical properties. In this section, we introduce some quantities, including *mass, energy, angular momentum expectation,* and *center of mass.* Their dynamical laws are briefly outlined and can be used as benchmarks for validating our method. Detailed proofs are provided in the appendixes.

Mass and energy. The time-dependent GPE (1.1)–(1.3) conserves two important quantities: the *mass* of the wave function and *the energy per particle,* i.e.,

$$\mathcal{N}(t) := \mathcal{N}(\psi(\cdot,t)) := \int_{\mathbb{R}^3} |\psi(\mathbf{x},t)|^2 \,\mathrm{d}\mathbf{x} \equiv \mathcal{N}(\psi(\cdot,0)) = 1, \quad t \geq 0, \tag{3.1}$$

and

$$\begin{aligned}\mathcal{E}(t) := \mathcal{E}(\psi(\cdot,t)) &= \int_{\mathbb{R}^3} \left[\frac{1}{2}|\nabla\psi|^2 + V|\psi|^2 + \frac{\beta}{2}|\psi|^4 + \frac{\lambda}{2}\Phi|\psi|^2 - \bar{\psi}(\boldsymbol{\Omega}\cdot\boldsymbol{L})\psi\right]\mathrm{d}\mathbf{x} \\ &\equiv \mathcal{E}(\psi(\cdot,0)), \quad t \geq 0.\end{aligned} \tag{3.2}$$

The detailed proof is provided in Appendix A.

Angular momentum expectation. The *angular momentum expectation* of the time-dependent GPE (1.1)–(1.3) is defined as $\langle \boldsymbol{L}\rangle(t) := \big(\langle L_x\rangle(t), \langle L_y\rangle(t), \langle L_z\rangle(t)\big)^\top$ with

$$\langle L_\alpha\rangle(t) = \int_{\mathbb{R}^3} \bar{\psi}(\mathbf{x},t) L_\alpha \psi(\mathbf{x},t)\mathrm{d}\mathbf{x}, \quad \alpha = x,y,z, \quad t \geq 0. \tag{3.3}$$

The angular momentum expectation can be used to measure the vortex flux. Its dynamics are described by the following lemma, with a detailed proof provided in Appendix B.

LEMMA 2. *For GPE* (1.1)–(1.3) *with harmonic potential* (1.5)*, the dynamics of angular momentum expectation is governed by the following ordinary differential equations (ODEs):*

$$\frac{d\langle L_x\rangle(t)}{dt} = (\gamma_y^2 - \gamma_z^2)\int_{\mathbb{R}^3} yz|\psi|^2\mathrm{d}\mathbf{x} - \omega_y\langle L_z\rangle + \omega_z\langle L_y\rangle - \lambda i\int_{\mathbb{R}^3}(L_x\Phi)|\psi|^2\mathrm{d}\mathbf{x}, \tag{3.4}$$

$$\frac{d\langle L_y\rangle(t)}{dt} = (\gamma_z^2 - \gamma_x^2)\int_{\mathbb{R}^3} zx|\psi|^2\mathrm{d}\mathbf{x} + \omega_x\langle L_z\rangle - \omega_z\langle L_x\rangle - \lambda i\int_{\mathbb{R}^3}(L_y\Phi)|\psi|^2\mathrm{d}\mathbf{x}, \tag{3.5}$$

$$\frac{d\langle L_z\rangle(t)}{dt} = (\gamma_x^2 - \gamma_y^2)\int_{\mathbb{R}^3} xy|\psi|^2\mathrm{d}\mathbf{x} - \omega_x\langle L_y\rangle + \omega_y\langle L_x\rangle - \lambda i\int_{\mathbb{R}^3}(L_z\Phi)|\psi|^2\mathrm{d}\mathbf{x}. \tag{3.6}$$

This demonstrates that the angular momentum expectation entry $\langle L_\alpha\rangle$ is conserved under certain parameters, that is,

$$\begin{aligned}&\langle L_x\rangle(t) \equiv \langle L_x\rangle(0), \quad t \geq 0, \quad \text{when } \gamma_y = \gamma_z,\ \omega_y = \omega_z = 0 \text{ and } \lambda = 0,\\ &\langle L_y\rangle(t) \equiv \langle L_y\rangle(0), \quad t \geq 0, \quad \text{when } \gamma_z = \gamma_x,\ \omega_z = \omega_x = 0 \text{ and } \lambda = 0,\\ &\langle L_z\rangle(t) \equiv \langle L_z\rangle(0), \quad t \geq 0, \quad \text{when } \gamma_x = \gamma_y,\ \omega_x = \omega_y = 0 \text{ and } \lambda = 0.\end{aligned}$$

Center of mass. The *center of mass* is defined as

$$\mathbf{x}_c(t) = \int_{\mathbb{R}^3} \mathbf{x}|\psi(\mathbf{x},t)|^2\mathrm{d}\mathbf{x}, \quad t \geq 0. \tag{3.7}$$

In particular, we have the following Lemma for its dynamics, and the proof can be found in Appendix C.

LEMMA 3. *For the GPE* (1.1)–(1.3) *with harmonic potential* (1.5)*, the dynamics of the center of mass satisfies the following second-order ODEs:*

$$\ddot{\mathbf{x}}_c(t) - 2A\dot{\mathbf{x}}_c(t) + (A^2 + S)\mathbf{x}_c(t) = 0, \quad t > 0, \tag{3.8}$$

$$\mathbf{x}_c(0) = \int_{\mathbb{R}^3} \mathbf{x}|\psi_0|^2 \mathrm{d}\mathbf{x}, \quad \dot{\mathbf{x}}_c(0) = A\mathbf{x}_c(0) + \int_{\mathbb{R}^3} \mathrm{Im}(\bar{\psi}_0 \nabla \psi_0)\mathrm{d}\mathbf{x}, \tag{3.9}$$

where $A = \begin{pmatrix} 0 & \omega_z & -\omega_y \\ -\omega_z & 0 & \omega_x \\ \omega_y & -\omega_x & 0 \end{pmatrix}$ *and* $S = \mathrm{diag}\{\gamma_x^2, \gamma_y^2, \gamma_z^2\}$.

4. Numerical result. In this section, we first test the spatial spectral accuracy for the DDI evaluation. Then, we verify the spatial and temporal accuracies for the wave function evolution. Subsequently, we explore the dynamical laws, including the evolution of mass, energy, angular momentum expectation, and center of mass. Finally, we investigate some interesting phenomena, such as the evolution of quantized vortices and dynamics of BEC under a honeycomb potential. In the following examples, we choose the computational domain $\mathbf{R}_L = [-8, 8]^3$ if not stated otherwise.

4.1. DDI evaluation. Here, we verify the spatial spectral accuracy of the FSA-base method. The numerical error is measured in the following norm:

$$e^{\mathrm{DDI}} := \|\Phi - \Phi_N\|_{l^2} / \|\Phi\|_{l^2} = \sqrt{\sum_{\mathbf{x}_{jk\ell} \in \mathcal{T}_N} |\Phi(\mathbf{x}_{jk\ell}) - \Phi_N(\mathbf{x}_{jk\ell})|^2} \Big/ \sqrt{\sum_{\mathbf{x}_{jk\ell} \in \mathcal{T}_N} |\Phi(\mathbf{x}_{jk\ell})|^2},$$

where Φ_N is the numerical solution on mesh grid $\mathcal{T}_N$, and Φ is the exact solution.

Example 1 (**DDI**). We consider 3D DDI with the following two types of source density:

- **Isotropic density**: we take Gaussian $\rho(\mathbf{x}) = e^{-|\mathbf{x}|^2/\sigma^2}$. The corresponding 3D DDI can be given explicitly as

$$\Phi(\mathbf{x}) = -\rho(\mathbf{x}) - 3\partial_{\mathbf{nn}} \left(\frac{\sigma^2 \sqrt{\pi}}{4} \frac{\mathrm{Erf}(|\mathbf{x}|/\sigma)}{|\mathbf{x}|/\sigma} \right),$$

  where $\mathrm{Erf}(x) = \frac{2}{\sqrt{\pi}} \int_0^x e^{-t^2} \mathrm{d}t$ is the error function.
- **Anisotropic density**: we take

$$\rho(\mathbf{x}) = \left(-\frac{4x^2}{\gamma^4 \sigma^4} - \frac{4y^2}{\sigma^4} - \frac{4z^2}{\sigma^4} + \frac{4}{\sigma^2} + \frac{2}{\gamma^2 \sigma^2} \right) e^{-\frac{x^2/\gamma^2 + y^2 + z^2}{\sigma^2}}.$$

  The corresponding 3D DDI can be given explicitly as

$$\Phi(\mathbf{x}) = -\rho(\mathbf{x}) - 3\partial_{\mathbf{nn}} \left(e^{-\frac{x^2/\gamma^2 + y^2 + z^2}{\sigma^2}} \right).$$

Table 1 presents errors of 3D DDI on the computational domain $\mathbf{R}_L = [-12\gamma, 12\gamma] \times [-12, 12]^2$ with different mesh sizes $\mathbf{h} := (\gamma h, h, h)$ for isotropic and anisotropic densities. For the isotropic case, we choose $\sigma = \sqrt{1.2}$ and $\varepsilon = 1$, while for the anisotropic case, we choose $\sigma = \sqrt{0.8}$ and $\varepsilon = 0.4$. Table 2 presents errors of 3D DDI with mesh size $h = 1/8$ under different anisotropy strengths γ, including cases where $\gamma \ll 1$ and $\gamma \gg 1$. From Table 1 and Table 2, it can be concluded that our method achieves spectral accuracy for both isotropic and anisotropic cases. Table 3 shows errors of 3D DDI with different dipole orientations $\mathbf{n} = (0.82778, 0.41505, -0.37751)^\top$ and $\mathbf{m} = (0.31180, 0.93780, -0.15214)^\top$, as described in Remark 2.5. From Table 3, it can be concluded that our method also achieves spectral accuracy when the two dipole orientations are different.

TABLE 1
Errors of 3D DDI with isotropic and anisotropic densities in Example 1.

Isotropic density				
	$h=2$	$h=1$	$h=1/2$	$h=1/4$
$\mathbf{n}=[0,0,1]^\top$	9.8224E-01	1.2809E-02	1.2673E-06	2.1021E-15
$\mathbf{n}=\frac{1}{\sqrt{3}}[1,1,1]^\top$	3.0243E+00	5.1071E-02	2.2608E-06	1.6395E-15
Anisotropic density ($\gamma=1/4$)				
	$h=1$	$h=1/2$	$h=1/4$	$h=1/8$
$\mathbf{n}=[0,0,1]^\top$	7.4342E-02	7.8062E-04	1.0355E-10	2.5596E-16
$\mathbf{n}=\frac{1}{\sqrt{3}}[1,1,1]^\top$	1.3888E+00	5.3973E-03	2.0272E-10	8.2313E-15

TABLE 2
Errors of 3D DDI with $\mathbf{n}=[0,0,1]^\top$ under different anisotropy strengths γ in Example 1.

$\gamma=1/16$	$\gamma=1/8$	$\gamma=1/4$	$\gamma=1/2$	$\gamma=8$	$\gamma=16$
1.1340E-16	1.6908E-16	2.5596E-16	5.7182E-16	4.0101E-15	6.5721E-15

TABLE 3
Errors of 3D DDI with different dipole orientations in Example 1.

$h=2$	$h=1$	$h=1/2$	$h=1/4$
2.4930	4.8379E-02	2.1322E-06	1.3589E-15

4.2. Accuracy confirmation. Here, we test the temporal and spatial convergence. For simplicity, we denote the second-order/fourth-order compact splitting as **CS2**/**CS4**. The numerical error is calculated in the following norm:

$$e^{h,\tau}(t) := \|\psi^{\mathrm{ref}}(t) - \psi^{(h,\tau)}(t)\|_{l^2} \ / \ \|\psi^{\mathrm{ref}}(t)\|_{l^2},$$

where $\psi^{(h,\tau)}(t)$ is the numerical approximation at time t obtained with mesh size h and time step τ, and $\psi^{\mathrm{ref}}(t)$ is the reference solution at time t. The corresponding temporal convergence rate is defined as follows:

$$\mathrm{rate} := \log(e^{h,\tau}/e^{h,\tau/2})/\log(2).$$

Example 2 (**linear case**). We test the temporal accuracy for linear subproblem solver EEI (2.12). We consider the following nonradially symmetric initial value

$$\psi^0(\mathbf{x}) = \frac{1}{\pi^{3/4}}\ x^2\ e^{-\frac{|\mathbf{x}|^2}{2}},$$

and the exact solution is expressed explicitly as

$$\psi(\mathbf{x},t) = \frac{1}{\pi^{3/4}}\frac{x_1^2(t)-t^2+it}{(1+it)^{7/2}} e^{-\frac{1}{2(it+1)}|\mathbf{x}|^2},$$

where $x_1(t) = x\cos(|\mathbf{\Omega}|t) + \frac{\sin(|\mathbf{\Omega}|t)}{|\mathbf{\Omega}|}(\omega_y z - \omega_z y) + \frac{1-\cos(|\mathbf{\Omega}|t)}{|\mathbf{\Omega}|^2}\omega_x(\mathbf{\Omega}\cdot\mathbf{x})$.

Table 4 presents the temporal errors of EEI at time $t=1$ with $h=1/4$ and $\tau=1$ for various $\mathbf{\Omega}$. The results clearly demonstrate that the EEI is *exact* in time.

Example 3 (**nonlinear case with/without DDI**). We verify the spectral accuracy in space and high-order temporal convergence. To this end, we choose $\mathbf{\Omega} = (0.1, 0.3, 0.5)^\top$, $\beta=10$, and the initial data $\psi^0(\mathbf{x}) = (x+iy)e^{-|\mathbf{x}|^2/2}/\pi^{3/4}$.

TABLE 4
Temporal errors $e^{h,\tau}$ at time $t=1$ for the EEI method in Example 2.

$\boldsymbol{\Omega}$	$(0.2,0.4,0.5)^\top$	$(0,0.4,0.2)^\top$	$(0.7,0.4,0.3)^\top$	$(0.7,0,0.6)^\top$
$e^{h,\tau}$	6.9231E-16	6.6777E-16	6.2787E-16	6.4059E-16

TABLE 5
Numerical errors of CS2 and CS4 at time $t=0.3$ in Example 3.

		Temporal direction			
	τ	1/20	1/40	1/80	1/160
CS2	$\lambda=0$	2.1457E-04	5.3421E-05	1.3341E-05	3.3338E-06
	rate		2.0060	2.0015	2.0006
	$\lambda=15/2$	1.9175E-04	4.7796E-05	1.1940E-05	2.9838E-06
	rate		2.0043	2.0011	2.0005
		Spatial direction			
	h	1	1/2	1/4	1/8
	$\lambda=0$	2.2891E-02	4.5467E-04	2.2500E-08	4.0938E-13
	$\lambda=15/2$	1.8344E-02	1.6892E-04	1.0112E-09	4.1119E-13
CS4		**Temporal** direction			
	τ	1/20	1/40	1/80	1/160
	$\lambda=0$	2.3710E-06	1.4459E-07	8.9930E-09	5.6149E-10
	rate		4.0355	4.0070	4.0015
	$\lambda=15/2$	2.9574E-06	1.8182E-07	1.1319E-08	7.0681E-10
	rate		4.0237	4.0057	4.0013
		Spatial direction			
	h	1	1/2	1/4	1/8
	$\lambda=0$	2.2891E-02	4.5467E-04	2.2500E-08	7.6492E-13
	$\lambda=15/2$	1.8344E-02	1.6892E-04	1.0112E-09	7.6486E-13

To verify the convergence of CS2/CS4, let ψ^{ref} denote the numerical reference solution computed using CS2/CS4 with very fine mesh size $h_0=1/16$ and small time step $\tau_0=10^{-4}$. Spatial errors are calculated using the same time step τ_0, and temporal errors are computed using the fixed mesh size h_0.

Table 5 presents the temporal and spatial errors of CS2 and CS4 at time $t=0.3$. From this table, one can see that CS2/CS4 exhibits the spatial *spectrally* accuracy and *second/fourth* order temporal convergence. A higher order operator splitting scheme is straightforward to design since both subproblems can be integrated exactly.

4.3. Dynamical properties verification. Here, we investigate the dynamical laws, including the evolution of mass, energy, angular momentum expectation, and center of mass.

Example 4 (**dynamics of mass, energy, and angular momentum expectation**). Here, we set $\beta=10$, and choose the initial value as

$$\psi^0(\mathbf{x})=\varphi(\mathbf{x}-\mathbf{x}_0),\quad \varphi(\mathbf{x})=\frac{1}{\pi^{4/3}}(x+iy)e^{-\frac{|\mathbf{x}|^2}{2}}. \tag{4.1}$$

We take $\mathbf{x}_0=(0.5,0.3,0.4)^\top$ and study the following five cases

- **Case i**: $\boldsymbol{\Omega}=(0.4,\ 0,\ 0)^\top$, $\boldsymbol{\gamma}=(1.1,\ 1,\ 1)^\top$, $\lambda=0$,
- **Case ii**: $\boldsymbol{\Omega}=(0.4,\ 0,\ 0)^\top$, $\boldsymbol{\gamma}=(1.1,\ 1,\ 1)^\top$, $\lambda=15$,
- **Case iii**: $\boldsymbol{\Omega}=(0,\ 0.4,\ 0)^\top$, $\boldsymbol{\gamma}=(1,\ 1.1,\ 1)^\top$, $\lambda=0$,
- **Case iv**: $\boldsymbol{\Omega}=(0,\ 0,\ 0.4)^\top$, $\boldsymbol{\gamma}=(1,\ 1,\ 1.1)^\top$, $\lambda=0$,
- **Case v**: $\boldsymbol{\Omega}=(0.1,\ 0.2,\ 0.3)^\top$, $\boldsymbol{\gamma}=(1,\ 1,\ 1)^\top$, $\lambda=0$,

where $\boldsymbol{\gamma}:=(\gamma_x,\gamma_y,\gamma_z)^\top$.

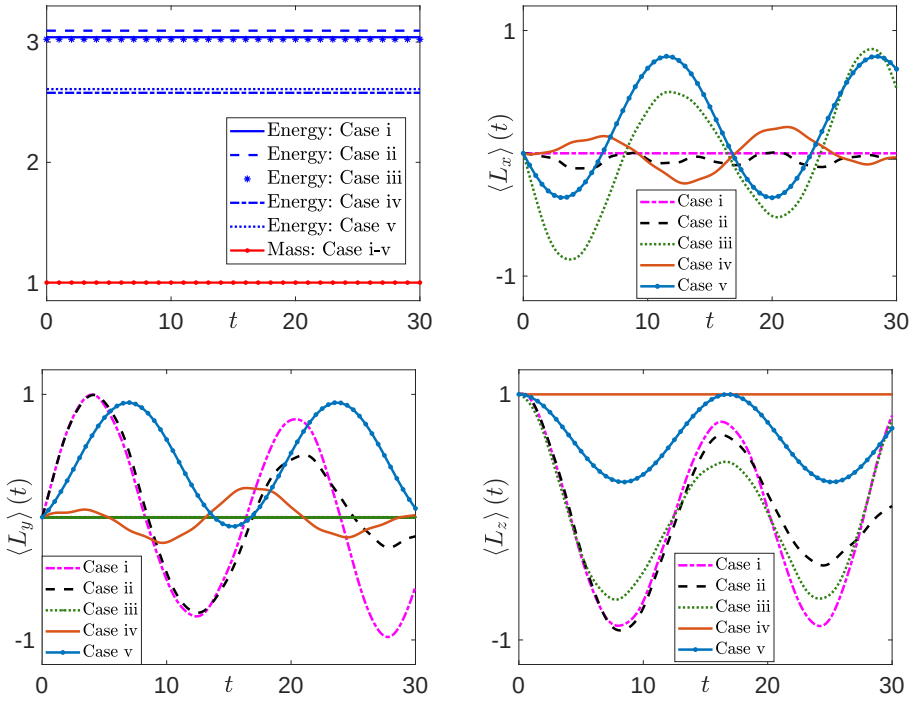

FIG. 2. *Evolution of energy* $\mathcal{E}(t)$*, mass* $\mathcal{N}(t)$*, and angular momentum expectation entries* $\langle L_\alpha \rangle(t)$ $(\alpha = x, y, z)$ *for* Case i–Case v *in Example* 4.

In Figure 2, we show the dynamics of energy $\mathcal{E}(t)$, mass $\mathcal{N}(t)$, and angular momentum expectation entries $\langle L_\alpha \rangle(t)$ $(\alpha = x, y, z)$ obtained numerically using CS4 with $h = 1/8$ and $\tau = 10^{-2}$ over the interval $t \in [0, 30]$. The results demonstrate that our method conserves the mass very well during the simulation, and these numerical observations align well with the analytical results.

Example 5 (**dynamics of center of mass**). Here, the initial data are taken as (4.1) with $\mathbf{x}_0 = (1, 1, 1)^\top$. We take $\beta = 50$ and $\lambda = 15$ and study the following three cases:

- **Case i**: $\boldsymbol{\gamma} = (1, 1, 1)^\top$, $\boldsymbol{\Omega} = (0, 0, 0)^\top, (0.5, 0, 0)^\top, (1, 0, 0)^\top, (\pi, 0, 0)^\top$,
- **Case ii**: $\boldsymbol{\gamma} = (1, 1, 1)^\top$, $\boldsymbol{\Omega} = \pi(0, 0, 1)^\top, \frac{\pi}{\sqrt{2}}(1, 1, 0)^\top, \frac{\pi}{\sqrt{2}}(1, 0, 1)^\top, \frac{\pi}{\sqrt{3}}(1, 1, 1)^\top$,
- **Case iii**: $\boldsymbol{\Omega} = (3, 4, 5)^\top$, $\boldsymbol{\gamma} = (1, 1, 1)^\top, (1.05, 1, 1)^\top, (1, 1.05, 1)^\top, (1, 1, 1.05)^\top$.

Figures 3–5 depict the trajectory of the center of mass $\mathbf{x}_c(t)$ and the evolution of its coordinates, calculated by the CS4 scheme with $h = 1/8$ and $\tau = 10^{-2}$ for different $\boldsymbol{\Omega}$ and $\boldsymbol{\gamma}$. In addition, the numerical results are compared with those obtained by solving the ODEs in (3.8)–(3.9).

From Figures 3–5, we can see that the center of mass remains confined within a bounded region if the external trap is symmetric, i.e., $\gamma_x = \gamma_y = \gamma_z$. Furthermore, the motion is periodic if the angular velocity $|\boldsymbol{\Omega}|$ is rational. When the external trap is not symmetric, the center of mass is more complicated. In addition, simulations not shown here for brevity confirm that the dynamics of the center of mass are independent of β and λ. These results are consistent with those obtained by solving the ODE system in (3.8)–(3.9).

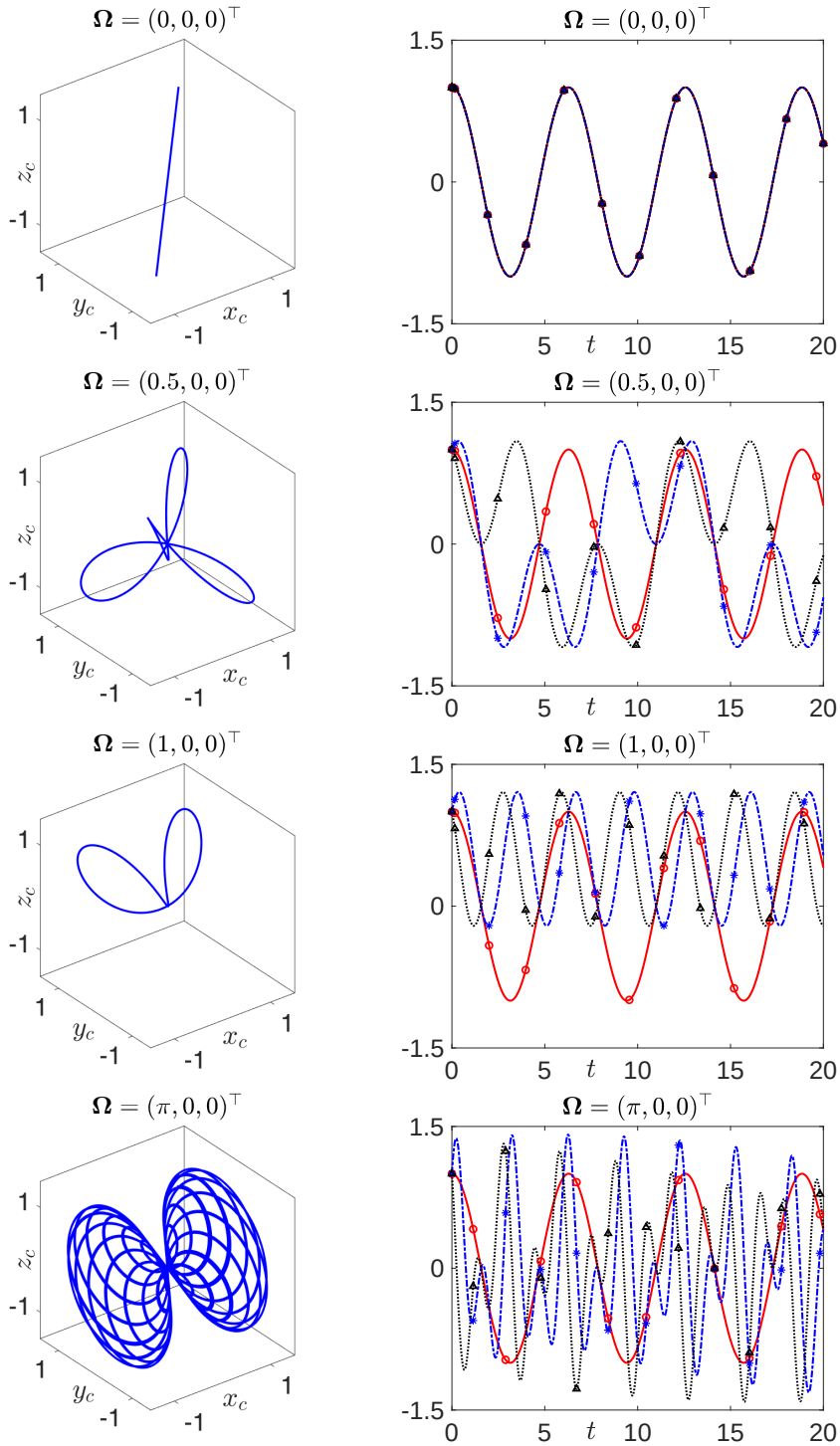

FIG. 3. *Motion of the center of mass* $\mathbf{x}_c(t) = (x_c(t), y_c(t), z_c(t))^\top$ *for* Case i *in Example* 5. *Left: trajectory* $\mathbf{x}_c(t)$ *for* $t \in [0, 100]$. *Right: time evolution of* $x_c(t)$ *(red solid line),* $y_c(t)$ *(blue dot line), and* $z_c(t)$ *(black dash line) that are obtained by directly simulating the GPE, where* o, $*$, *and* $\triangle$ *represent the solutions to the ODEs in* (3.8)–(3.9).

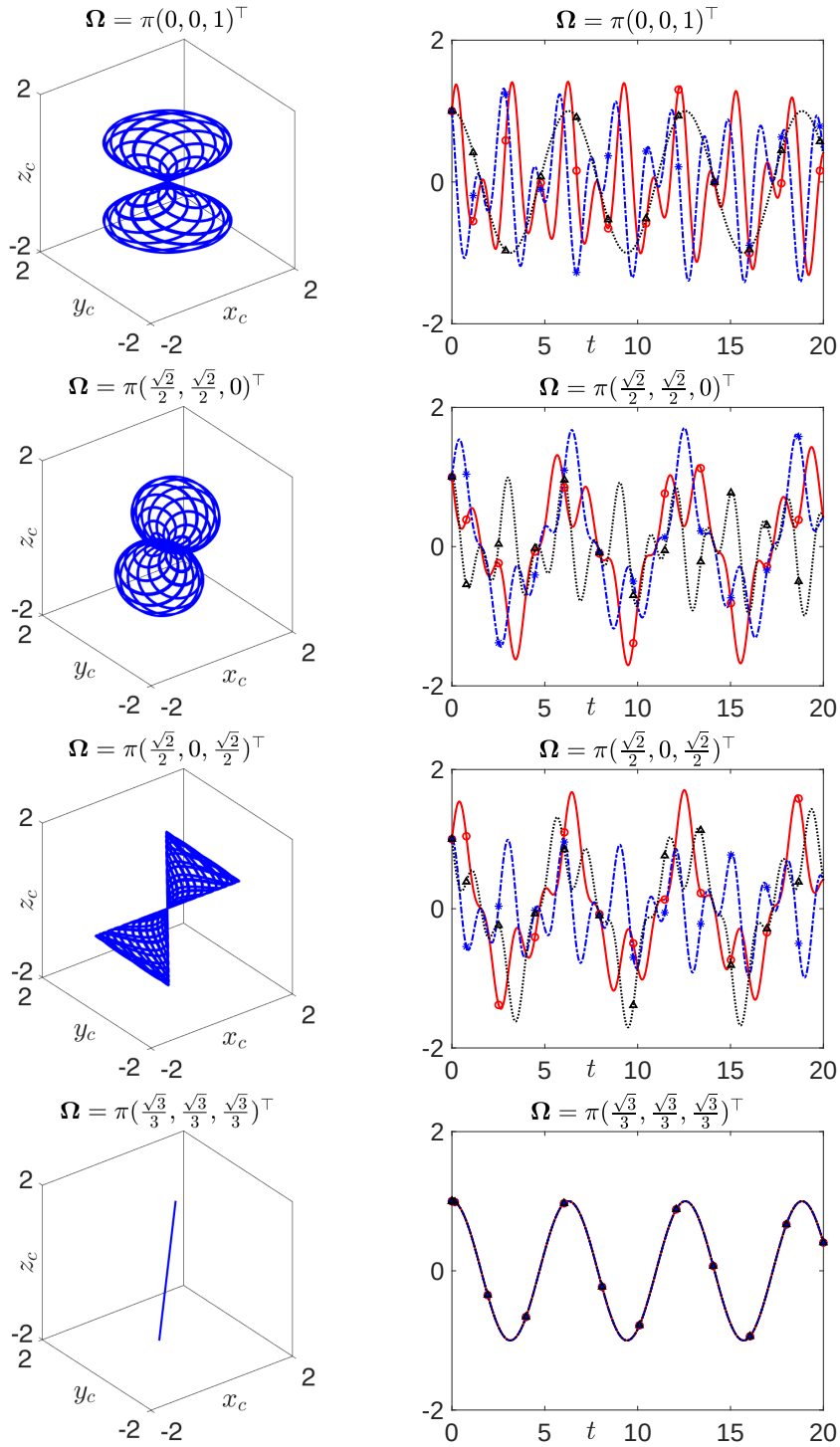

FIG. 4. *Motion of the center of mass* $\mathbf{x}_c(t) = (x_c(t), y_c(t), z_c(t))^\top$ *for* Case ii *in Example* 5. *Left: trajectory* $\mathbf{x}_c(t)$ *for* $t \in [0, 100]$. *Right: time evolution of* $x_c(t)$ *(red solid line),* $y_c(t)$ *(blue dot line), and* $z_c(t)$ *(black dash line) that are obtained by directly simulating the GPE, where* o, $*$, *and* $\triangle$ *represent the solutions to the ODEs in* (3.8)–(3.9).

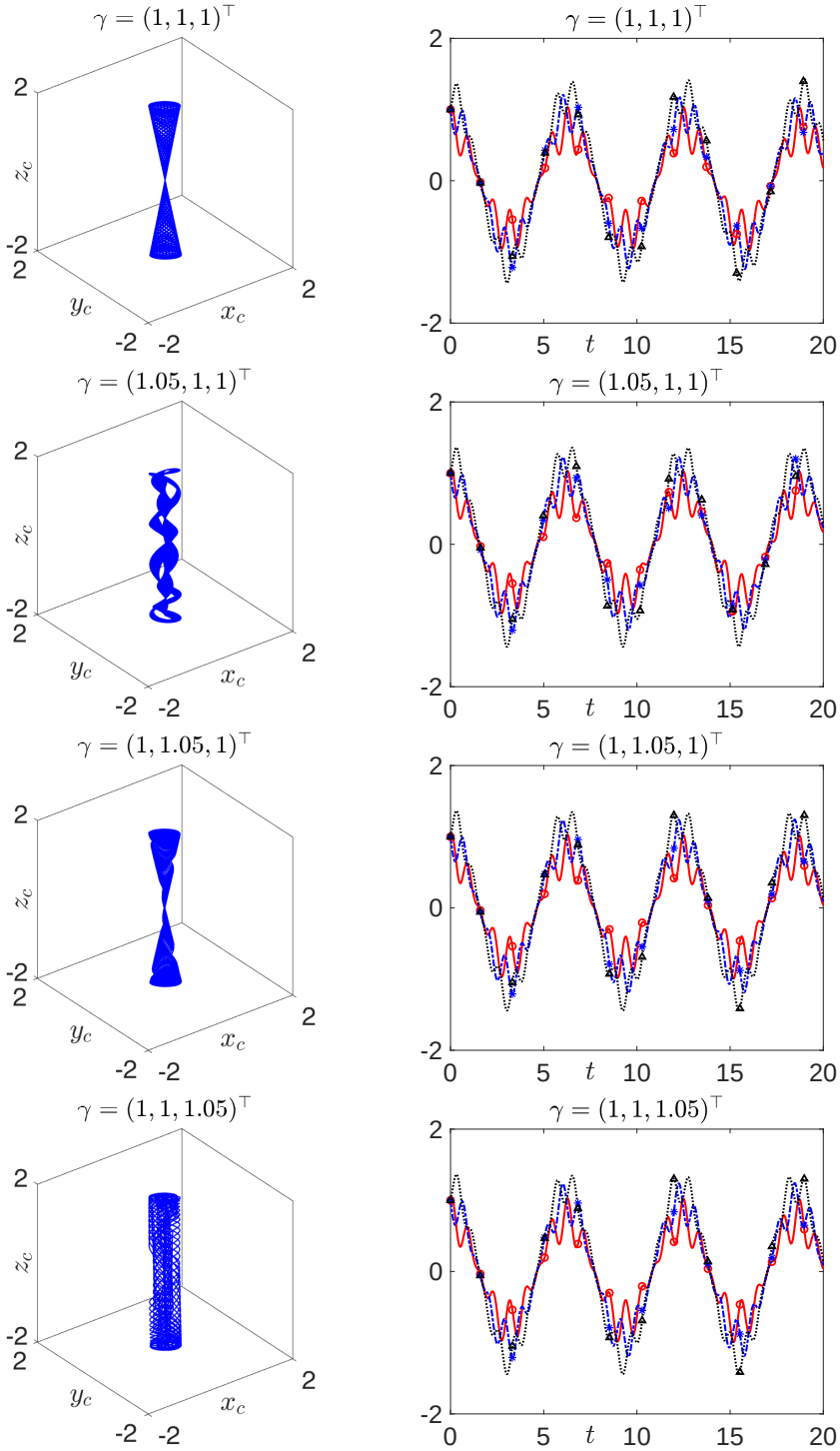

FIG. 5. *Motion of the center of mass* $\mathbf{x}_c(t) = (x_c(t), y_c(t), z_c(t))^\top$ *for* Case iii *in Example* 5. *Left: trajectory* $\mathbf{x}_c(t)$ *for* $t \in [0, 100]$. *Right: time evolution of* $x_c(t)$ *(red solid line),* $y_c(t)$ *(blue dot line), and* $z_c(t)$ *(black dash line) that are obtained by directly simulating the GPE, where* o, $*$, *and* $\triangle$ *represent the solutions to the ODEs in* (3.8)–(3.9).

4.4. Applications. In the following, we study the interaction of quantized vortices and dynamics under honeycomb potential.

Example 6 (**dynamics of quantized vortices**). Here, we set $\mathbf{\Omega} = (0.85, 0, 0)^\top$, $\beta = 100$, $\lambda = 50$, and choose the harmonic potential (1.5) with $\gamma_x = \gamma_y = \gamma_z = 1$. The initial value is taken as a stationary vortex state computed by the preconditioned Riemannian conjugate gradient method [31] for the above parameters, with the corresponding energy $\mathcal{E} = 2.5021$. The interactions of vortices are investigated for the following two cases:

- **Case i**: perturb the external potential by setting $\gamma_x = 1.4$, $\gamma_y = 0.7$,
- **Case ii**: perturb the rotation term by setting $\mathbf{\Omega} = (0, 0.85, 0)^\top$.

In our simulations, we take $\mathbf{R}_L = [-16, 16]^3$, $N = 256$, and $\tau = 10^{-3}$. Figure 6 presents the isosurface plots of the densities $|\psi|^2 = 10^{-3}$ computed by CS4 at different times for Case i and Case ii. We see that during the dynamics, anisotropic compression occurs due to the anisotropic external potential, and the vortices rotate to form different patterns because of the rotation term.

Example 7 (**dynamics under honeycomb potential**). Here, we choose $\mathbf{\Omega} = (0.1, 0.2, 0.3)^\top$, $\beta = 10$, $\lambda = 15/2$, and the initial data $\psi(\mathbf{x}) = (x + iy)e^{-|\mathbf{x}|^2/2}/\pi^{3/4}$. We study the dynamics under honeycomb potential

$$V(\mathbf{x}) = 10\left[\cos(\boldsymbol{b_1}\cdot\mathbf{x}) + \cos(\boldsymbol{b_2}\cdot\mathbf{x}) + \cos((\boldsymbol{b_1}+\boldsymbol{b_2})\cdot\mathbf{x})\right],$$

where $\boldsymbol{b_1} = \frac{\pi}{4}(\sqrt{3}, 1)^\top$ and $\boldsymbol{b_2} = \frac{\pi}{4}(-\sqrt{3}, 1)^\top$.

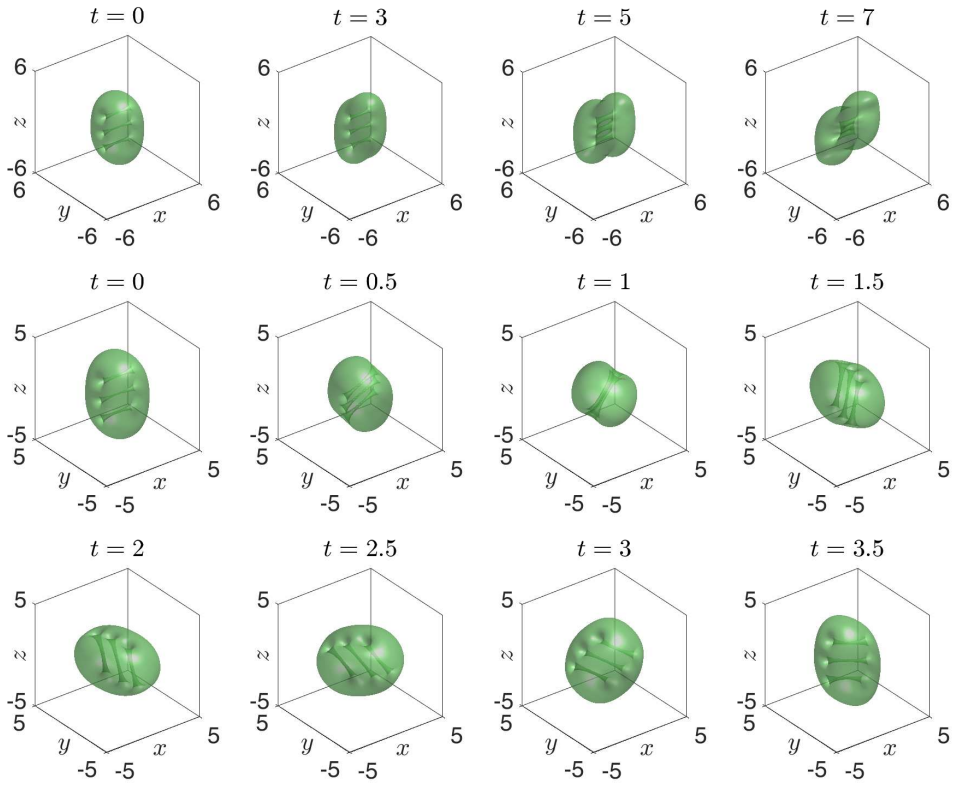

FIG. 6. *Isosurface plots of* $|\psi|^2 = 10^{-3}$ *for the dynamics of quantized vortices for* Case i *(top one row) and* Case ii *(bottom two rows) in Example* 6.

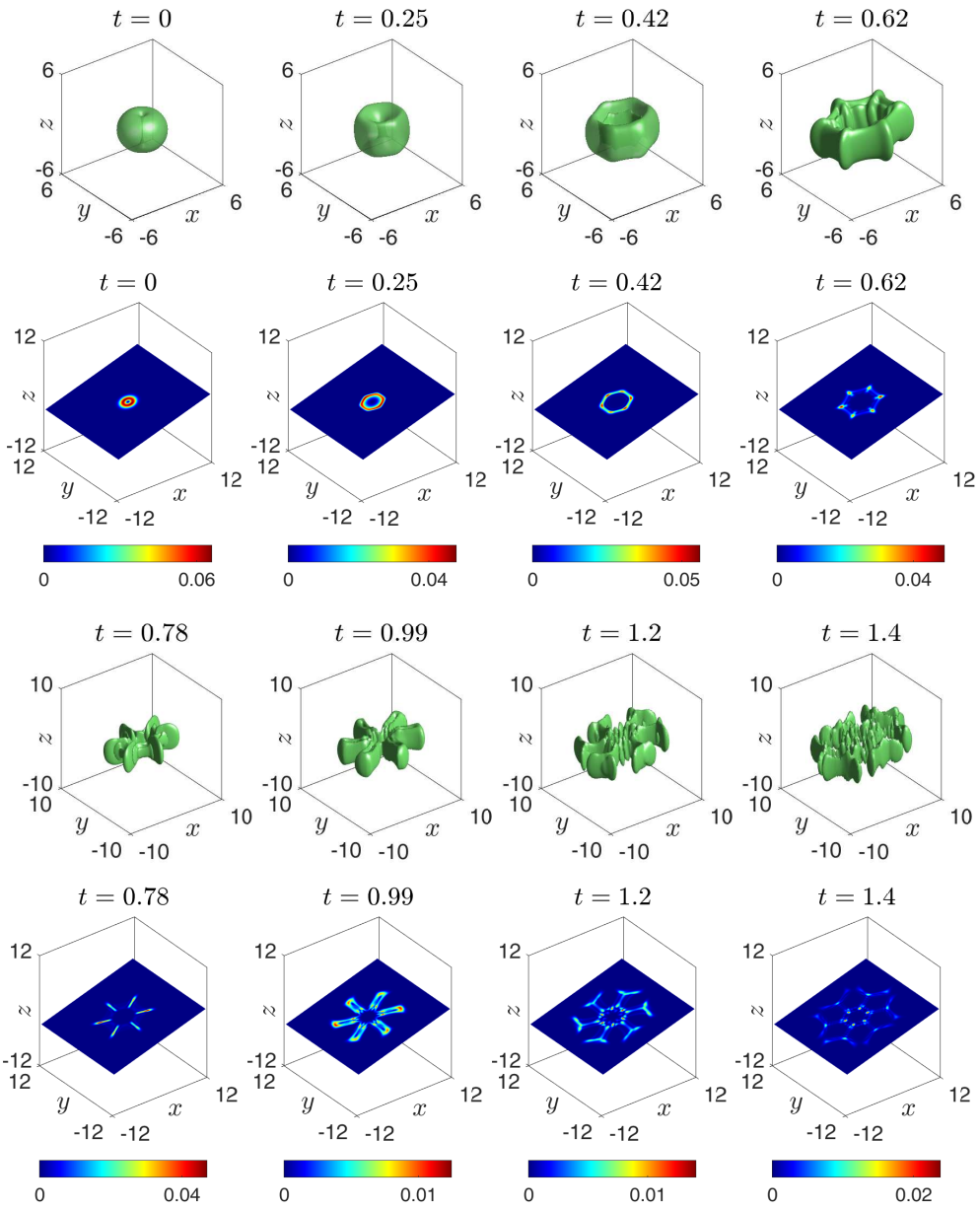

FIG. 7. *Isosurface and slice plots of the densities* $|\psi|^2 = 10^{-3}$ *in Example* 7.

In our simulation, we adopt the CS4 scheme with $\tau = 10^{-3}$ and $h = 1/16$. Figure 7 shows the isosurface and slice plots of the densities $|\psi|^2 = 10^{-3}$ at different times.

5. Conclusions. We developed high-order numerical schemes to simulate the dynamics of dipolar BEC with arbitrary-angle rotation. The Hamiltonian is split into a linear part (Laplace and rotation) and nonlinear part (all others terms). The linear subproblem is integrated exactly by decomposing the linear operator into a product of seven simple suboperators with analytical splitting coefficients. The nonlinear

subproblem is solved exactly in physical space, and the DDI is computed using a FSA-based method with spectral accuracy, achieving nearly optimal efficiency and requiring minimum memory. Based on such compact splitting, we can easily construct high-order spectral methods to simulate the dynamics. Our scheme achieves high-order temporal convergence and spatial spectral accuracy, and it conserves the mass on discrete level (unconditionally stable). Extensive numerical results demonstrate the effectiveness in long-time simulations. Furthermore, our scheme is explicit, simple to implement, and can be easily adapted to rotating dipolar systems, including scalar or spinor BECs.

Appendix A. Proof of mass and energy conservation.

Proof. To prove mass conservation, we differentiate (3.1) with respect to time t. Using equation (1.1), we have

$$\begin{aligned}\frac{d\mathcal{N}(t)}{dt} &= \int_{\mathbb{R}^3} \partial_t\psi\,\bar{\psi} + \psi\,\partial_t\bar{\psi}\ \mathrm{d}\mathbf{x} = 2\ \mathrm{Im}\int_{\mathbb{R}^3} i\partial_t\psi\,\bar{\psi}\ \mathrm{d}\mathbf{x}\\ &= 2\ \mathrm{Im}\int_{\mathbb{R}^3} -\big[(\boldsymbol{\Omega}\cdot\boldsymbol{L})\psi\big]\bar{\psi}\ \mathrm{d}\mathbf{x} = 2\ \mathrm{Im}\int_{\mathbb{R}^3} \psi\big[(\boldsymbol{\Omega}\cdot\boldsymbol{L})\bar{\psi}\big]\ \mathrm{d}\mathbf{x}\\ &= 2\ \mathrm{Im}\int_{\mathbb{R}^3} \overline{-\big[(\boldsymbol{\Omega}\cdot\boldsymbol{L})\psi\big]\bar{\psi}}\ \mathrm{d}\mathbf{x} = 0.\end{aligned}$$

Similarly, for energy conservation, we can prove that

$$\begin{aligned}\frac{d\mathcal{E}(t)}{dt} &= \int_{\mathbb{R}^d} \frac{\delta\mathcal{E}}{\delta\psi}\,\partial_t\psi + \frac{\delta\mathcal{E}}{\delta\bar{\psi}}\,\partial_t\bar{\psi}\ \mathrm{d}\mathbf{x} = 2\ \mathrm{Re}\int_{\mathbb{R}^d} \frac{\delta\mathcal{E}}{\delta\bar{\psi}}\,\partial_t\bar{\psi}\ \mathrm{d}\mathbf{x}\\ &= 2\ \mathrm{Re}\int_{\mathbb{R}^d} i\partial_t\psi\,\partial_t\bar{\psi}\ \mathrm{d}\mathbf{x} = 2\ \mathrm{Re}\int_{\mathbb{R}^d} i|\partial_t\psi|^2\ \mathrm{d}\mathbf{x} = 0.\end{aligned}$$

The proof is completed. ∎

Appendix B. Proof of Lemma 2.

Proof. Differentiating (3.3) with respect to t, using (1.1) and integration by parts, we have

$$\begin{aligned}\frac{d\langle L_\alpha\rangle(t)}{dt} &= \int_{\mathbb{R}^3} \big[(\partial_t\bar{\psi})\ (L_\alpha\psi) + \bar{\psi}\ L_\alpha(\partial_t\psi)\big]\,\mathrm{d}\mathbf{x}\\ &= i\int_{\mathbb{R}^3} -(L_\alpha V)|\psi|^2 - \lambda(L_\alpha\Phi)|\psi|^2 + [(\boldsymbol{\Omega}\cdot\boldsymbol{L})\psi](L_\alpha\psi) + \bar{\psi}[L_\alpha(\boldsymbol{\Omega}\cdot\boldsymbol{L})\psi]\ \mathrm{d}\mathbf{x}.\end{aligned}$$

When $\alpha = x$, using $L_xL_y = L_yL_x + iL_z$ and $L_xL_z = L_zL_x - iL_y$, we have $L_xV = i(\gamma_y^2 - \gamma_z^2)yz$ and

$$\begin{aligned}&\int_{\mathbb{R}^3} [(\boldsymbol{\Omega}\cdot\boldsymbol{L})\psi](L_x\psi) + \bar{\psi}[L_x(\boldsymbol{\Omega}\cdot\boldsymbol{L})\psi]\ \mathrm{d}\mathbf{x}\\ &= \omega_y\int_{\mathbb{R}^3} (L_y\psi)(L_x\psi) + \bar{\psi}(L_xL_y\psi)\ \mathrm{d}\mathbf{x} + \omega_z\int_{\mathbb{R}^3} (L_z\psi)(L_x\psi) + \bar{\psi}(L_xL_z\psi)\ \mathrm{d}\mathbf{x}\\ &= \omega_y\int_{\mathbb{R}^3} (L_y\psi)(L_x\psi) + \bar{\psi}(L_yL_x + iL_z\psi)\mathrm{d}\mathbf{x} + \omega_z\int_{\mathbb{R}^3} (L_z\psi)(L_x\psi) + \bar{\psi}(L_zL_x - iL_y\psi)\mathrm{d}\mathbf{x}\\ &= i\omega_y\int_{\mathbb{R}^3} \bar{\psi}L_z\psi\ \mathrm{d}\mathbf{x} - i\omega_z\int_{\mathbb{R}^3} \bar{\psi}L_y\psi\ \mathrm{d}\mathbf{x} = i\big[\omega_y\langle L_z\rangle(t) - \omega_z\langle L_y\rangle(t)\big].\end{aligned}$$

Then, (3.4) holds. Similarly, for $\alpha = y$ and z, (3.5) and (3.6) hold. The proof is completed. ∎

Appendix C. Proof of Lemma 3.

Proof. Differentiating (3.7) with respect to t, using (1.1) and integration by parts, we obtain

$$\begin{aligned}\frac{d\mathbf{x}_c(t)}{dt} &= \int_{\mathbb{R}^3} \mathbf{x}\left[(\partial_t\bar{\psi})\psi + \bar{\psi}(\partial_t\psi)\right]\mathrm{d}\mathbf{x} = -i\int_{\mathbb{R}^3} \bar{\psi}\ \nabla\psi + \left[(\boldsymbol{\Omega}\cdot\boldsymbol{L})\mathbf{x}\right]|\psi|^2\ \mathrm{d}\mathbf{x}\\ &= A\int_{\mathbb{R}^3} \mathbf{x}|\psi|^2\mathrm{d}\mathbf{x} - i\int_{\mathbb{R}^3} \bar{\psi}\ \nabla\psi\ \mathrm{d}\mathbf{x} = A\mathbf{x}_c(t) - i\int_{\mathbb{R}^3} \bar{\psi}\ \nabla\psi\ \mathrm{d}\mathbf{x}, \end{aligned} \tag{C.1}$$

where $A = \begin{pmatrix} 0 & \omega_z & -\omega_y \\ -\omega_z & 0 & \omega_x \\ \omega_y & -\omega_x & 0 \end{pmatrix}$. Differentiating (C.1) with respect to t, we have

$$\begin{aligned}\frac{d^2\mathbf{x}_c(t)}{dt^2} - A\frac{d\mathbf{x}_c(t)}{dt} &= -i\int_{\mathbb{R}^3} (\partial_t\bar{\psi})\nabla\psi + \bar{\psi}\ \nabla(\partial_t\psi)\\ &= -\int_{\mathbb{R}^3} (\nabla V)|\psi|^2\mathrm{d}\mathbf{x} + \int_{\mathbb{R}^3} \left[(\boldsymbol{\Omega}\cdot\boldsymbol{L})\bar{\psi}\right]\nabla\psi + \bar{\psi}\left[\nabla(\boldsymbol{\Omega}\cdot\boldsymbol{L})\psi\right]\mathrm{d}\mathbf{x}\\ &= -S\int_{\mathbb{R}^3} \mathbf{x}|\psi|^2\mathrm{d}\mathbf{x} + \int_{\mathbb{R}^3} \left[(\boldsymbol{\Omega}\cdot\boldsymbol{L})\bar{\psi}\right]\nabla\psi + \bar{\psi}\left[(\boldsymbol{\Omega}\cdot\boldsymbol{L})\nabla - iA\nabla\right]\psi\mathrm{d}\mathbf{x}\\ &= -S\mathbf{x}_c(t) - iA\int_{\mathbb{R}^3} \bar{\psi}\ \nabla\psi\mathrm{d}\mathbf{x} = -S\mathbf{x}_c(t) + A\frac{d\mathbf{x}_c(t)}{dt} - A^2\mathbf{x}_c(t), \end{aligned}$$

where $S = \mathrm{diag}\{\gamma_x^2, \gamma_y^2, \gamma_z^2\}$. Then, we can get the ODEs (3.8)–(3.9), and the proof is completed. ∎

REFERENCES

[1] J. R. Abo-Shaeer, C. Raman, J. M. Vogels, and W. Ketterle, *Observation of vortex lattices in Bose-Einstein condensates*, Science, 292 (2001), pp. 476–479, https://doi.org/10.1126/science.1060182.

[2] K. Aikawa, A. Frisch, M. Mark, S. Baier, A. Rietzler, R. Grimm, and F. Ferlaino, *Bose-Einstein condensation of Erbium*, Phys. Rev. Lett., 108 (2012), 210401, https://doi.org/10.1103/PhysRevLett.108.210401.

[3] M. H. Anderson, J. R. Ensher, M. R. Matthewa, C. E. Wieman, and E. A. Cornell, *Observation of Bose-Einstein condensation in a dilute atomic vapor*, Science, 269 (1995), pp. 198–201, https://doi.org/10.1126/science.269.5221.198.

[4] X. Antoine, W. Bao, and C. Besse, *Computational methods for the dynamics of the nonlinear Schrödinger/Gross-Pitaevskii equations*, Comput. Phys. Commun., 184 (2013), pp. 2621–2633, https://doi.org/10.1016/j.cpc.2013.07.012.

[5] W. Bao and Y. Cai, *Mathematical theory and numerical methods for Bose-Einstein condensation*, Kinet. Relat. Models, 6 (2013), pp. 1–135, https://doi.org/10.3934/krm.2013.6.1.

[6] W. Bao, Q. Du, and Y. Zhang, *Dynamics of rotating Bose-Einstein condensates and its efficient and accurate numerical computation*, SIAM J. Appl. Math., 66 (2006), pp. 758–786, https://doi.org/10.1137/050629392.

[7] W. Bao, H. Li, and J. Shen, *A generalized-Laguerre-Fourier-Hermite pseudospectral method for computing the dynamics of rotating Bose-Einstein condensates*, SIAM J. Sci. Comput., 31 (2009), pp. 3685–3711, https://doi.org/10.1137/080739811.

[8] W. Bao, D. Marahrens, Q. Tang, and Y. Zhang, *A simple and efficient numerical method for computing the dynamics of rotating Bose-Eeinstein condensates via rotating Lagrangian coordinates*, SIAM J. Sci. Comput., 35 (2013), pp. A2671–A2695, https://doi.org/10.1137/130911111.

[9] W. Bao and H. Wang, *An efficient and spectrally accurate numerical method for computing dynamics of rotating Bose-Einstein condensates*, J. Comput. Phys., 217 (2006), pp. 612–626, https://doi.org/10.1016/j.jcp.2006.01.020.

[10] J. Bernier, *Exact splitting methods for semigroups generated by inhomogeneous quadratic differential operators*, Found. Comput. Math., 21 (2021), pp. 1401–1439, https://doi.org/10.1007/s10208-020-09487-4.

[11] J. Bernier, N. Crouseilles, and Y. Li, *Exact splitting methods for kinetic and Schrödinger equations*, J. Sci. Comput., 86 (2021), pp. 1–35, https://doi.org/10.1007/s10915-020-01369-9.

[12] C. Besse, G. Dujardin, and I. Lacroix-Violet, *High order exponential integrators for nonlinear Schrödinger equations with application to rotating Bose-Einstein condensates*, SIAM J. Numer. Anal., 55 (2017), pp. 1387–1411, https://doi.org/10.1137/15M1029047.

[13] Q. Chauleur, R. Chicircanu, G. Dujardin, J.-C. Garreau, and A. Rançon, *Numerical Study of the Gross-Pitaevskii Equation on a Two-dimensional Ring and Vortex Nucleation*, arXiv:2404.10360, 2024.

[14] I. Danaila and F. Hecht, *A finite element method with mesh adaptivity for computing vortex states in fast-rotating Bose-Einstein condensates*, J. Comput. Phys., 229 (2010), pp. 6946–6960, https://doi.org/10.1016/j.jcp.2010.05.032.

[15] L. Exl, N. J. Mauser, and Y. Zhang, *Accurate and efficient computation of nonlocal potentials based on Gaussian-sum approximation*, J. Comput. Phys., 327 (2016), pp. 629–642, https://doi.org/10.1016/j.jcp.2016.09.045.

[16] L. Greengard, S. Jiang, and Y. Zhang, *The anisotropic truncated kernel method for convolution with free-space Green's functions*, SIAM J. Sci. Comput., 40 (2018), pp. A3733–A3754, https://doi.org/10.1137/18M1184497.

[17] A. Griesmaier, J. Werner, S. Hensler, J. Stuhler, and T. Pfau, *Bose-Einstein condensation of Chromium*, Phys. Rev. Lett., 94 (2005), 160401, https://doi.org/10.1103/PhysRevLett.94.160401.

[18] P. Henning and A. Målqvist, *The finite element method for the time-dependent Gross-Pitaevskii equation with angular momentum rotation*, SIAM J. Numer. Anal., 55 (2017), pp. 923–952, https://doi.org/10.1137/15M1009172.

[19] S. Jiang, L. Greengard, and W. Bao, *Fast and accurate evaluation of nonlocal Coulomb and dipole-dipole interactions via the nonuniform FFT*, SIAM J. Sci. Comput., 36 (2014), pp. 777–794, https://doi.org/10.1137/130945582.

[20] T. Lahaye, C. Menotti, L. Santos, M. Lewenstein, and T. Pfau, *The physics of dipolar bosonic quantum gases*, Rep. Prog. Phys., 72 (2009), 126401, https://doi.org/10.1088/0034-4885/72/12/126401.

[21] X. Liu, X. Meng, Q. Tang, and Y. Zhang, *High-order compact splitting spectral methods for the rotating spin-*1 *Bose-Einstein condensates in a magnetic field*, Math. Models Methods Appl. Sci., 35 (2025), pp. 2013–2045, https://doi.org/10.1142/S0218202525500253.

[22] X. Liu, Q. Tang, S. Zhang, and Y. Zhang, *On optimal zero-padding of kernel truncation method*, SIAM J. Sci. Comput., 46 (2024), pp. A23–A49, https://doi.org/10.1137/23M1550803.

[23] X. Liu, Y. Yuan, and Y. Zhang, *An efficient compact splitting Fourier spectral method for computing the dynamcis of rotating spin-orbit coupled spin-1 Bose-Einstein condensates*, J. Comput. Phys., 529 (2025), 113892, https://doi.org/10.1016/j.jcp.2025.113892.

[24] X. Liu and Y. Zhang, *Fast Convolution Solver Based on Far-Field Smooth Approximation*, arXiv:2504.19410, 2025.

[25] M. Lu, N. Q. Burdick, S. H. Youn, and B. L. Lev, *Strongly dipolar Bose-Einstein condensate of Dysprosium*, Phys. Rev. Lett., 107 (2011), 190401, https://doi.org/10.1103/PhysRevLett.107.190401.

[26] R. I. McLachlan and G. R. W. Quispel, *Splitting methods*, Acta Numer., 11 (2002), pp. 341–434, https://doi.org/10.1017/S0962492902000053.

[27] S. B. Prasad, B. C. Mulkerin, and A. M. Martin, *Arbitrary-angle rotation of the polarization of a dipolar Bose-Einstein condensate*, Phys. Rev. A, 103 (2021), 033322, https://doi.org/10.1103/PhysRevA.103.033322.

[28] S. B. Prasad, B. C. Mulkerin, and A. M. Martin, *Stationary states, dynamical stability, and vorticity of Bose-Einstein condensates in tilted rotating harmonic traps*, Phys. Rev. A, 101 (2020), 063608, https://doi.org/10.1103/PhysRevA.101.063608.

[29] J. Shen, T. Tang, and L. Wang, *Spectral Methods: Algorithms, Analysis and Applications*, Springer, 2011.

[30] Q. Shu, Q. Tang, Y. Yuan, and Y. Zhang, *An efficient numerical method for the dynamics of arbitrary-angle rotating Bose-Einstein condensates via orthogonal coordinate transformation*, to be submitted.

[31] Q. Shu, Q. Tang, S. Zhang, and Y. Zhang, *A preconditioned Riemannian conjugate gradient method for computing the ground states of arbitrary-angle rotating Bose-Einstein condensates*, J. Comput. Phys., 512 (2024), 113130, https://doi.org/10.1016/j.jcp.2024.113130.

[32] N. L. Smith, W. H. Heathcote, J. M. Krueger, and C. J. Foot, *Experimental observation of the tilting mode of an array of vortices in a dilute Bose-Einstein condensate*, Phys. Rev. Lett., 93 (2004), 080406, https://doi.org/10.1103/PhysRevLett.93.080406.

[33] R. M. van Bijnen, A. J. Dow, D. H. J. O'Dell, N. G. Parker, and A. M. Martin, *Exact solutions and stability of rotating dipolar Bose-Einstein condensates in the Thomas-Fermi limit*, Phys. Rev. A, 80 (2009), 033617, https://doi.org/10.1103/PhysRevA.80.033617.

[34] F. Vico, L. Greengard, and M. Ferrando, *Fast convolution with free-space Green's functions*, J. Comput. Phys., 323 (2016), pp. 191–203, https://doi.org/10.1016/j.jcp.2016.07.028.

[35] H. Wang, J. Wang, S. Zhang, and Y. Zhang, *A time splitting Chebyshev-Fourier spectral method for the time-dependent rotating nonlocal Schrödinger equation in polar coordinates*, J. Comput. Phys., 498 (2024), 112680, https://doi.org/10.1016/j.jcp.2023.112680.

[36] H. Yoshida, *Construction of higher order symplectic integrators*, Phys. Lett. A, 150 (1990), pp. 262–268, https://doi.org/10.1016/0375-9601(90)90092-3.